NATIONAL AERONAUTICS AND SPACE ADMINISTRATION

Technical Report 32-1357

Transonic Dynamic and Static Stability Characteristics of Three Blunt-Cone Planetary Entry Shapes

Wayne J. Marko

JET PROPULSION LABORATORY
CALIFORNIA INSTITUTE OF TECHNOLOGY
PASADENA, CALIFORNIA

September 1, 1969

NATIONAL AERONAUTICS AND SPACE ADMINISTRATION

Technical Report 32-1357

Transonic Dynamic and Static Stability Characteristics of Three Blunt-Cone Planetary Entry Shapes

Wayne J. Marko

JET PROPULSION LABORATORY
CALIFORNIA INSTITUTE OF TECHNOLOGY
PASADENA, CALIFORNIA

September 1, 1969

Prepared Under Contract No. NAS 7-100
National Aeronautics and Space Administration

Preface

The work described in this report was performed by the Environmental Sciences Division of the Jet Propulsion Laboratory.

Acknowledgment

This experimental program was successfully concluded through the cooperation of the Experimental Investigations Branch of the NASA Ames Research Center and its contractor, ARO Inc. Particular recognition is due employees of the Jet Propulsion Laboratory E. Adams and W. Fife for work in test preparations vital to the success of this program, P. Jaffe for advice concerning data acquisition and analysis, and photographer D. Maxeiner for the excellent quality of film data obtained.

Contents

Tables

Figures

Contents (contd)

Figures (contd)

Abstract

An investigation of the dynamic stability characteristics of three high-drag planetary entry shapes (spherically blunted 60- and 70-deg-half-angle cones) has been conducted in the 6×6-ft supersonic wind tunnel of the Ames Research Center at transonic speeds. Free-flight testing techniques were successfully used to document the effects of Mach number and oscillation amplitudes on the transonic dynamic stability of the principal shape, the sharp-edged 60-deg-half-angle cone. Two primary results were observed from the test. First, transonic dynamic stability coefficients are not as unfavorable (destabilizing) as those previously reported in open literature. However, the decrease in dynamic stability in the transonic regime compared with that in the subsonic and supersonic regimes continues to be significant. Second and most important, the transonic dynamic stability is shown to be dependent on oscillation amplitude. As the effective oscillation amplitude decreased, the dynamic stability became more unfavorable. This effect was observed as highly convergent amplitude envelopes for effective amplitudes greater than 15 deg, and as divergent envelopes for amplitudes below 10 deg. The use of these dynamic stability data in computer simulations of entry into the tenuous atmosphere of Mars by a hypothesized entry capsule is demonstrated. Static coefficients obtained as a by-product of the dynamic investigation are also presented.

Transonic Dynamic and Static Stability Characteristics of Three Blunt-Cone Planetary Entry Shapes

I. Introduction

The angular motions of an atmospheric entry vehicle with respect to its flight path are of concern for the following reasons: (1) amplitude-dependent aerodynamic loads during entry must be known at the time of design; (2) aerodynamic heating will vary over the vehicle surface as a function of amplitude; and (3) operational functions such as payload or decelerator deployment, or communications could be seriously affected by vehicle oscillation. The dynamic stability characteristics of several atmospheric entry vehicles of conical shape have been investigated experimentally throughout the Mach number range. However, it seemed that the available data had not completely defined their transonic dynamic stability characteristics. Theoretical analysis of the dynamic stability characteristics of high-drag bodies in the transonic speed regime is at best difficult. Consequently, experimental transonic dynamic stability data are of considerable interest and importance.

In an effort to better define the transonic dynamic stability of high-drag entry shapes, an experimental program was initiated that would use the free-flight technique in the 6×6-ft supersonic wind tunnel of the Ames Research Center. The free-flight technique has most of the advantages of the ballistic range while eliminating many of its limitations, particularly in the area of model design, and number of data points obtained per flight.

This report describes the experimental transonic dynamic stability investigation and resulting aerodynamic coefficients.[1] Model design, launching methods and equipment, data acquisition, and data reduction are discussed. Test data are presented for one 70- and two 60-deg-half-angle cones through the Mach number range of 0.54 to 2.0 at a test Reynolds number of 0.312×10^6 based on the 1.5-in. model diameter. A 60-deg sharp-edged cone was the most thoroughly tested of the three configurations, in that the effects of both oscillation amplitude and Mach number were considered. Both static and dynamic stability as well as drag are presented as functions of amplitude and of Mach number. These data are used in computer simulations of capsule entry into an assumed Mars atmosphere. Planar motion histories of amplitude envelopes for a nonspinning 60-deg-half-angle cone are presented. These results were also reported in part in Ref. 1.

[1]The raw motion data of the models from which these test data were obtained are presented in report SR 900-297. This publication is available upon request to J. Jackson, Technical Information and Documentation Division, Jet Propulsion Laboratory

II. Test Facility and Free-Flight Technique

Tests were conducted in the Ames 6 × 6-ft supersonic wind tunnel without modifications to the facility. It is a closed-circuit, single-return type of tunnel with an asymmetric sliding-block nozzle and a test section with perforated floor and ceiling. The possibility of pressure disturbances affecting the data was minimized by the sizing of the model to 1.5 in. in diameter so that during flight the minimum distance to the model from any side of the 6 × 6-ft test section was 23.5 in. with a blockage ratio of less than 0.04% (ratio of model frontal area to wind tunnel test-section area).

Over a period of several years, the Jet Propulsion Laboratory (JPL) has developed testing techniques to study the motion of axisymmetric aerodynamic shapes in free flight. These techniques, reported at various meetings and symposia, are fundamentally the ones used in this investigation and are well documented in Refs. 2 through 5. The free-flight models were launched opposite the airstream direction at velocities up to 250 ft/s relative to the test section. The release of the models approximately 8 in. downstream of the viewing area assured that they were free of interference from the launcher while in the viewing area. Although a pneumatic launcher was available for use in the 6 × 6-ft facility, two important hardware modifications were made to this equipment. A pneumatically operated trigger was substituted for a piston-shaft restraining cable and guillotine squib. Previously, the restraining cable limited the forward travel of the piston and shaft until the cable was severed by the guillotine squib, which was fired electrically. A balsa cylinder was substituted for a tapered aluminum sleeve that had previously been used to absorb the kinetic energy of the piston shaft. Other modifications were made to the launcher. The original steel piston and shaft were replaced with aluminum parts. The shaft was now hollow, and the piston was made in several parts with Teflon seals sandwiched between. The changes in design reduced moving mass which, in turn, increased model acceleration and reduced the piston-shaft deceleration loads.

The piston seals assured a reservoir of pressure before launch and reduced sliding friction. A linear ball bearing mounted in the forward part of the launcher also helped to reduce friction. The completed launcher is shown in Fig. 1.

The propellant lines and controller circuit of the launcher are shown in Fig. 2. The launch of the model and the camera operation were controlled sequentially by a timer. When the desired wind tunnel conditions were reached just before the launch, the restraining fingers of the model were opened pneumatically and the propellant pressure necessary to project the model to the forward part of the viewing area was established in the launcher reservoir. Starting the launch sequence brought the camera to speed (4500 frames/s) followed by the operation of the solenoid-controlled ball valve and subsequent retraction of the trigger pin. The model was then launched into the viewing area of the test section. The purpose of the relay circuit was to hold the high-pressure valve solenoid in the activated position until it was reset manually.

Figure 3 shows the pneumatic launcher mounted in the 6 × 6-ft wind tunnel on the pitch strut sting body. A 60-deg-half-angle cone model is mounted on the front of the launcher with the restraining fingers holding the model in place.

The launcher was calibrated for speeds up to its maximum of 250 ft/s (Fig. 4). The propellant used to operate the launcher and valves was gaseous nitrogen. However, high-pressure compressed air would have also been a satisfactory alternate propellant.

A sketch of the balsa cylinder used to bring the piston shaft to rest from 250 ft/s is shown in Fig. 5. The 7-in.-long balsa cylinder was positioned with the grain running parallel to the shaft and was crushed to approximately 2 in. in length. It provided adequate energy absorption in the available distance, and was inexpensive, easily handled, and readily turned to the desired shape. In addition, the density of the wood could be chosen to accommodate different combinations of piston-shaft mass and velocity. Here, wood of 8 to 10 lb/ft^3 was used. Balsa used as a crushable material is discussed in Ref. 6. The cylinder was slotted on the end that contacted the piston, to help initiate crushing and reduce peak loads on the shaft.

Although the pneumatic launch gun presented some of the most difficult problems encountered during test preparations, some of the other pieces of equipment used in the test are essential to the success of this type of a free-flight experiment and are, therefore, described. The location of some of these pieces of equipment as well as the general layout of the Ames 6 × 6-ft test section area is shown in Fig. 6. No extensive modifications were made to the facility in the test installation. However, the small first-surface mirror in the schlieren

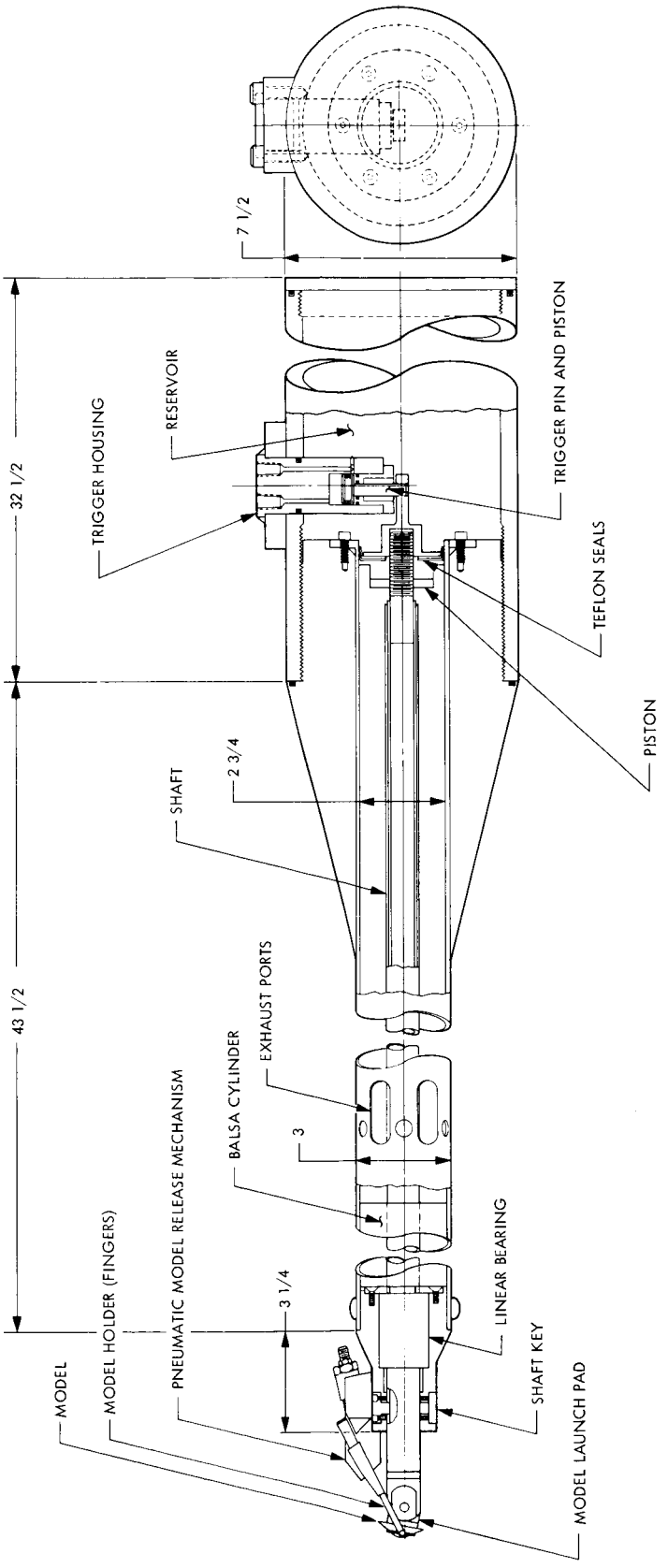

Fig. 1. Pneumatic launcher with modifications

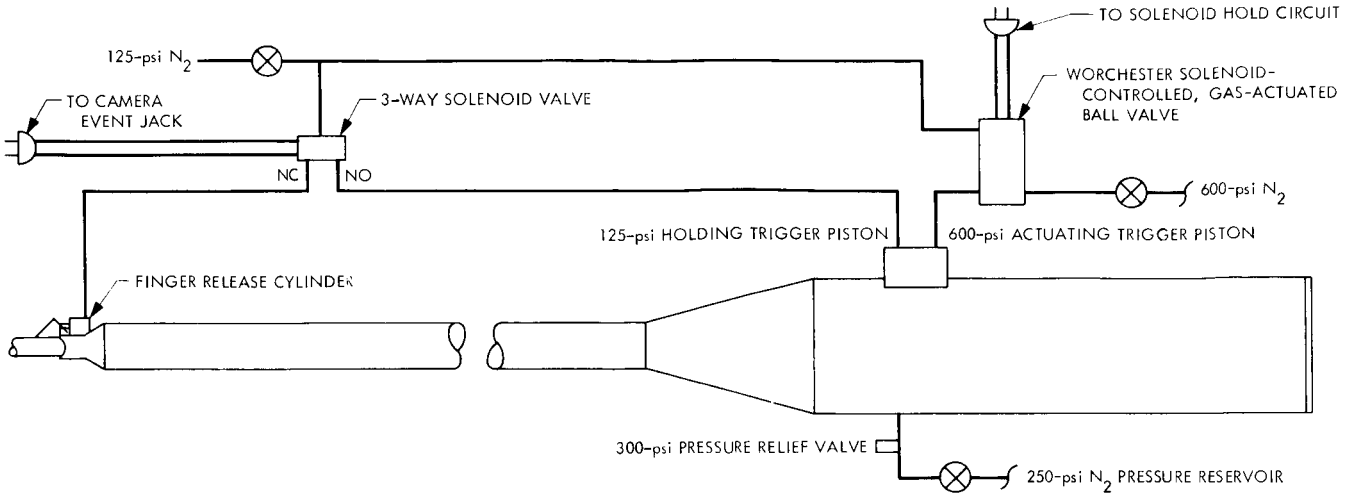

LAUNCH GUN PLUMBING

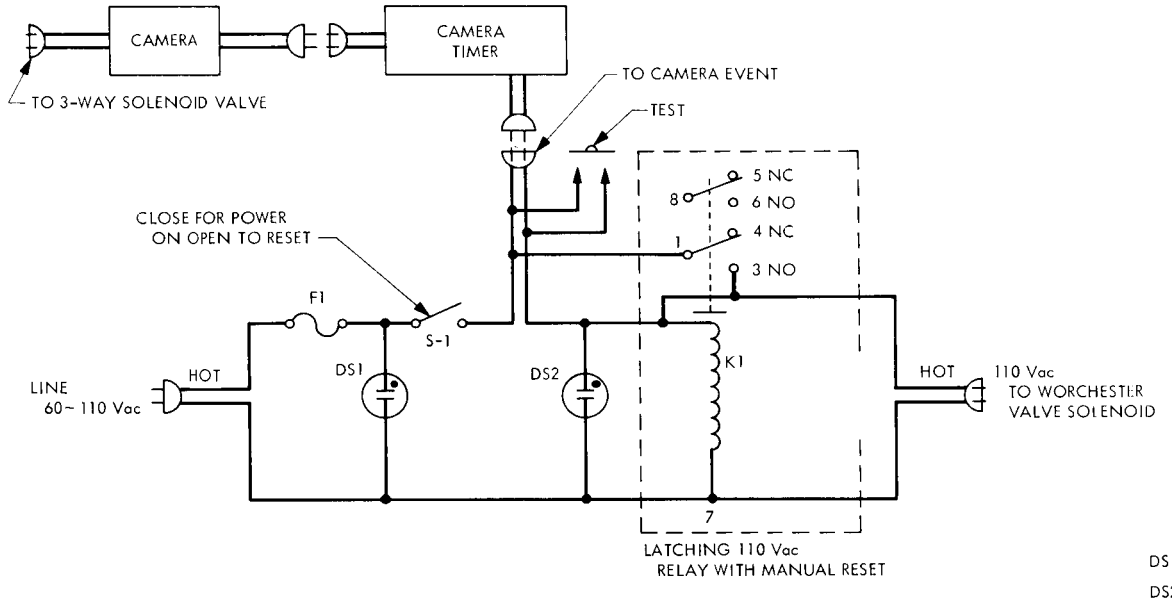

LAUNCH GUN SOLENOID HOLD CIRCUIT

LATCHING RELAY

PARTS	
DS1	NE 51 GREEN
DS2	NE 51 RED
F1	5A
S1	SP 51
K1	KRP-11A6 110 Vac 60~

Fig. 2. Launcher pneumatic system and latching relay

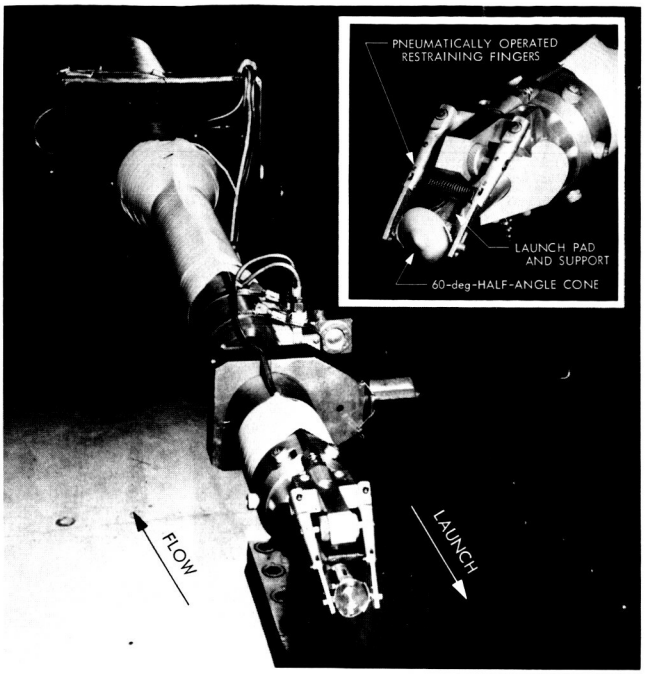

Fig. 3. Launcher installed in Ames 6 x 6-ft supersonic wind tunnel

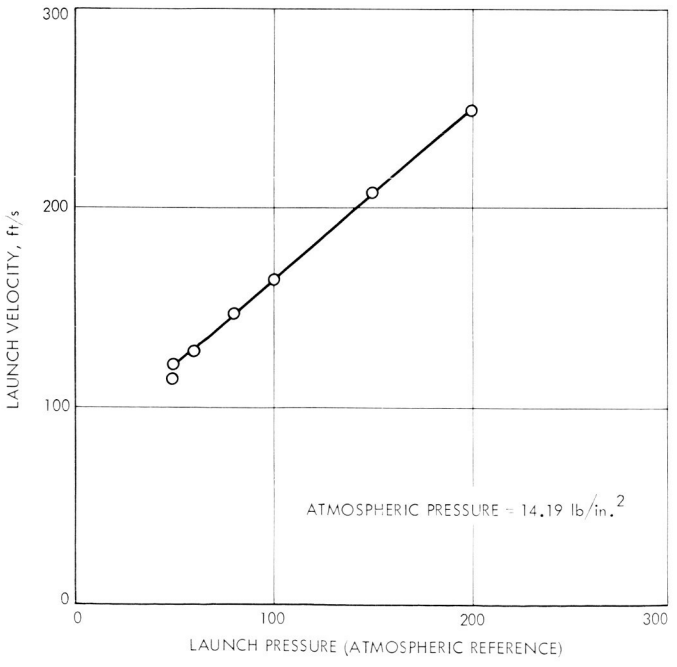

Fig. 4. Launcher calibration

optical system and the existing light-source bulb were removed. Removal of the mirror allowed positioning of an adjustable knife edge (translation in three mutually orthogonal axes) and high speed motion picture camera in the schlieren path.

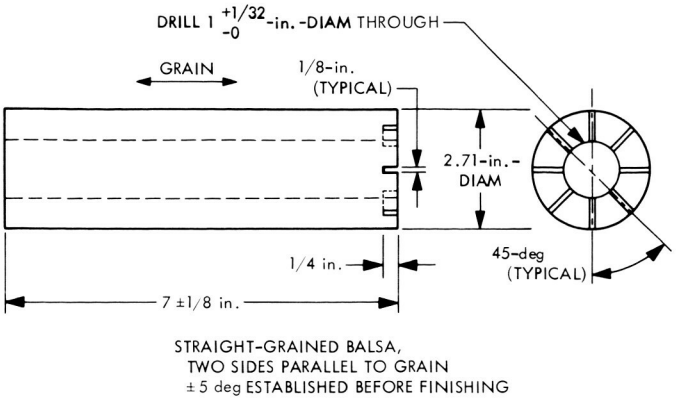

Fig. 5. Balsa decelerator

Of primary importance was the light source and its power supply, which provided stop motion photography. A multiflash stroboscopic light of 0.2-μs duration was used in these tests. It was synchronized with the high speed 35-mm motion picture camera and power for the light source was supplied by an EG&G Inc.[2] Type 501 stroboscopic power supply. The stroboscopic bulb was located in the existing light-source housing (Fig. 6) by means of a simple integral bracket and reflector.

A precision wire grid (not shown) was clamped to the frame of the viewing window on the camera side of the test section. Wire, 0.020 in. in diameter, was strung horizontally and vertically on the frame at 2.0-in. ($\pm$0.005) centers predetermined when the frame was machined. The grid provides a reference to be used when the film data are reduced to aerodynamic coefficients.

A 35-mm half-frame Fastax camera was used in these tests. The camera was mounted on a tripod with the lens coincident with the schlieren light path. It was equipped with a reluctance pickup to synchronize the stroboscopic light with the shutter, and a timing light to mark the film at 0.001-s intervals to provide a time base for data reduction. The lens plate thickness had been reduced by 0.125 in. to enable the focusing of the 6-in. camera lens to a point beyond infinity. The reason for this requirement is stated in detail in Ref. 7; basically, it stems from the fact that the light source and the model image do not emanate from the same location. Photographs were taken through the wind tunnel schlieren system, thereby eliminating parallax distortions and providing a continuous flow field record. A sequence of

[2]Edgerton, Germeshausen & Grier, Inc., 160 Brookline Ave., Boston, Mass., 02215.

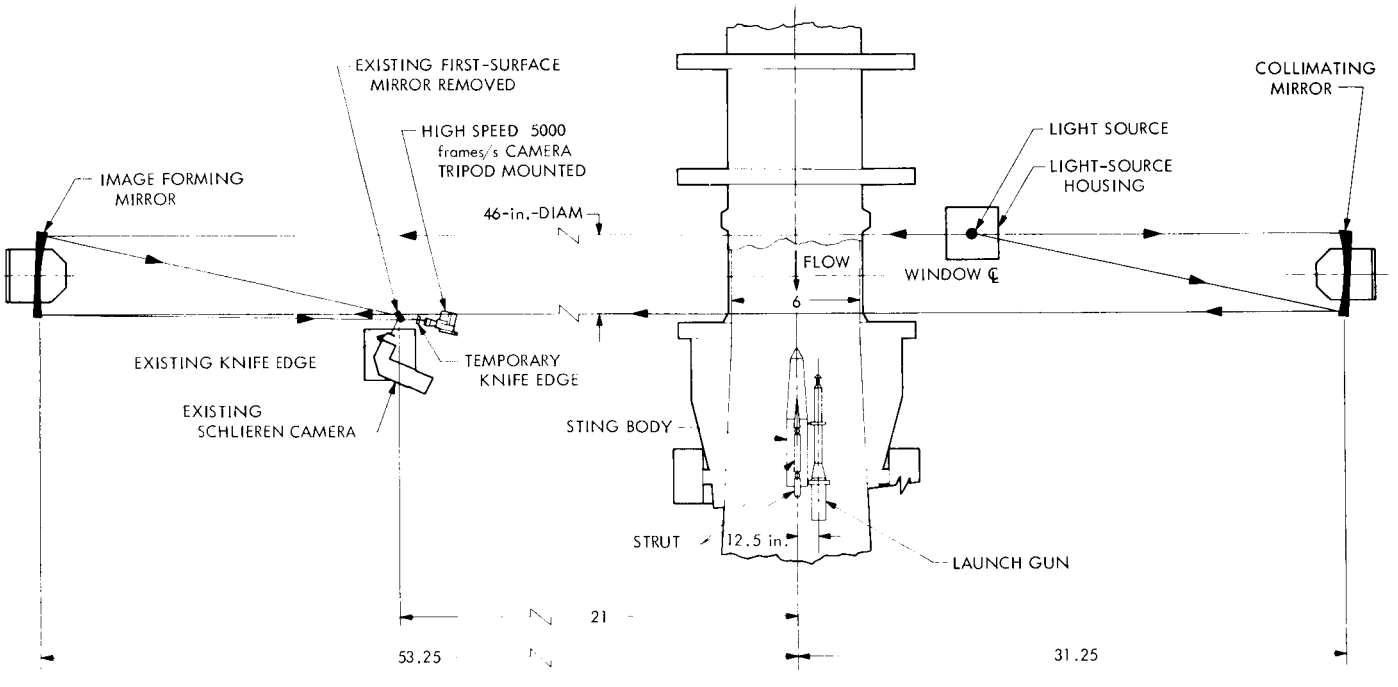

ALL DIMENSIONS ARE IN FEET
UNLESS OTHERWISE SPECIFIED

Fig. 6. Plan view of 6 x 6-ft test section area and equipment location

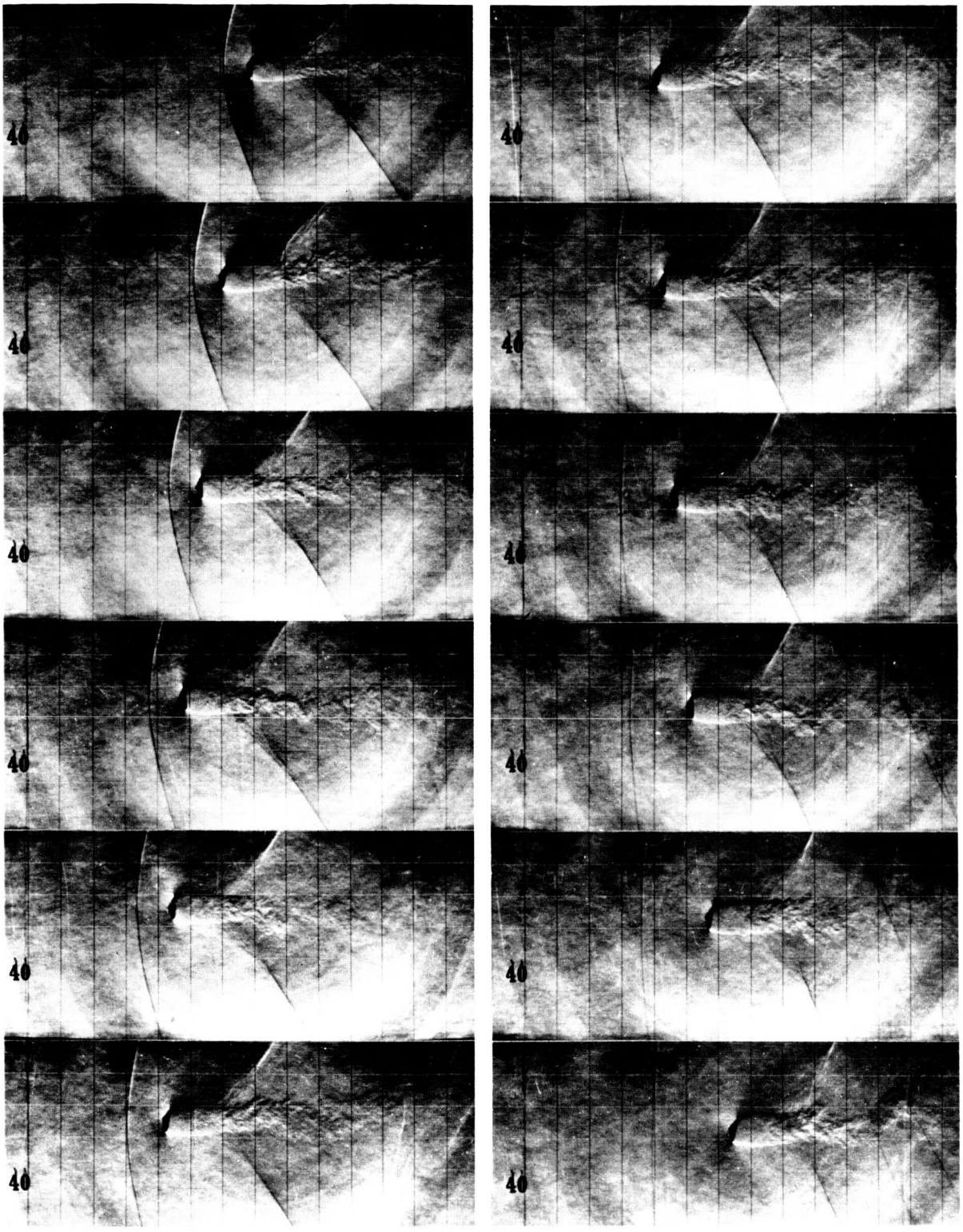

Fig. 7. Schlieren sequence of a 60-deg cone in free flight at $M_\infty = 1.06$

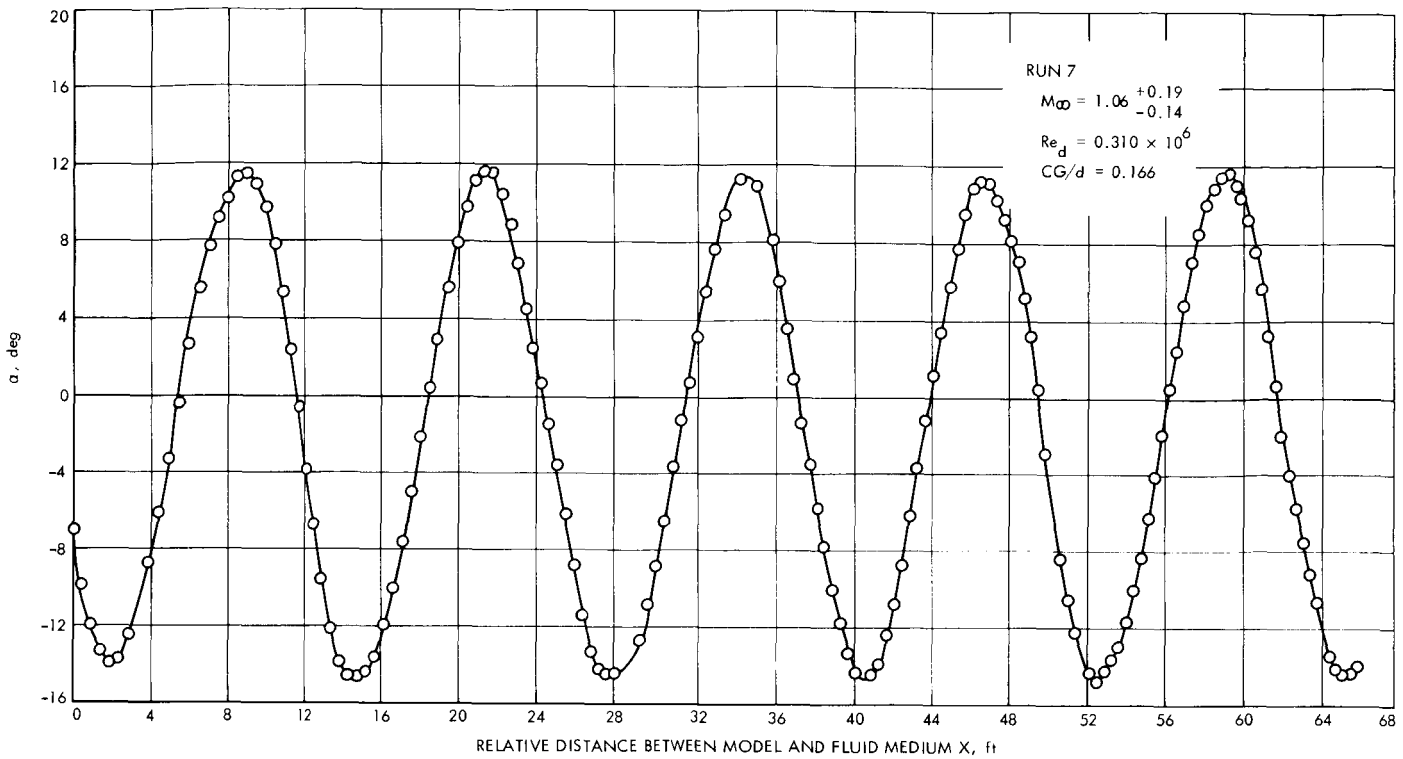

Fig. 8. Typical angle-of-attack history

selected high speed motion picture frames is shown in Fig. 7 and a typical angle-of-attack history is plotted in Fig. 8 from film data readings. This particular angle-of-attack history is interesting, for it shows a flight (run 7) at constant-peak angle of attack over a wide range of Mach numbers (1.25 to 0.92).

III. Free-Flight Model Design

The design of a free-flight model is somewhat complicated when oscillatory data are required. Moreover, an additional restraint is added when testing in a closed-circuit tunnel with an axial flow compressor downstream of the diffuser. The model must be of such construction, size, and weight that no damage to the compressor blades will ensue. For this application, the model was made to disintegrate on impact with any solid object before reaching the compressor blades. Catching the model in one piece is a less desirable alternative. Not only has it proved difficult to capture a free-flight model in such a facility, but such equipment as scoops or screens needed to catch the model might degrade the flow characteristics, and increase the possibility of tunnel blockage. The accuracy of dynamic stability data depends on (1) amplitude decay per cycle, and (2) number of oscillation cycles recorded during the flight. Proper model design maximizes these parameters by decreasing the size of the model while holding the mass distribution fixed. This causes the number of observed oscillations to increase while the decay remains the same. There is, however, a lower limit to the minimum size of a model imposed by the photographic resolution and model physical construction limitations. A model diameter of 1.5 in. was chosen, using the criteria mentioned.

Previous design practice (Ref. 2) was used to maximize the frequency of oscillation for a given model weight by building a thin model shell of polystyrene plastic weighted with a core of gold or lead. However, a solid core, such as gold or lead, does not disintegrate on impact. A powdered metal, namely tungsten, was suggested by Ames personnel for this experiment. The densities of gold, lead, and tungsten are

Lead	0.410 lb/in.^{3}
Gold (22k)	0.653 lb/in.^{3}
Tungsten	0.697 lb/in.^{3}

Gold and tungsten, with similar densities, each have advantages. Because gold is malleable and is easier than tungsten to machine and cast, it is preferred when it can be recovered. However if recovery is impossible, as

in the case of a destructible model, tungsten is preferred because of its lower cost.

The model shell was constructed of two or three pieces of molded polystyrene plastic as shown in Fig. 9. The method of construction is described in Ref. 2. The forward aeroshell included a small cup in the shape of the intended ballast. The second piece was composed of a disk that sealed the back of the model and the cup when glued in place.

After some practice, the ballasts were simply cast. Tungsten powder of four grain sizes was mixed with water and the resulting slurry poured into the ballast cup; the material was packed as the cup was filled. The water was drawn off by placing the model in a vacuum oven at 100°F and applying a hard vacuum. The proportions of the tungsten powder used for the tests were these:

8 measures	0.020 to 0.030-in.-diam
5 measures	100 μ
3 measures	10 μ
1 measure	1 μ

The resulting packed mixture had a density of approximately 74% of solid tungsten. Using four grain sizes, rather than a single size, limited the air spaces in the core and produced a higher model mass and mass to moment of inertia ratio. The compacted mass of nonuniform-size particles appeared to form a hard interlocking structure

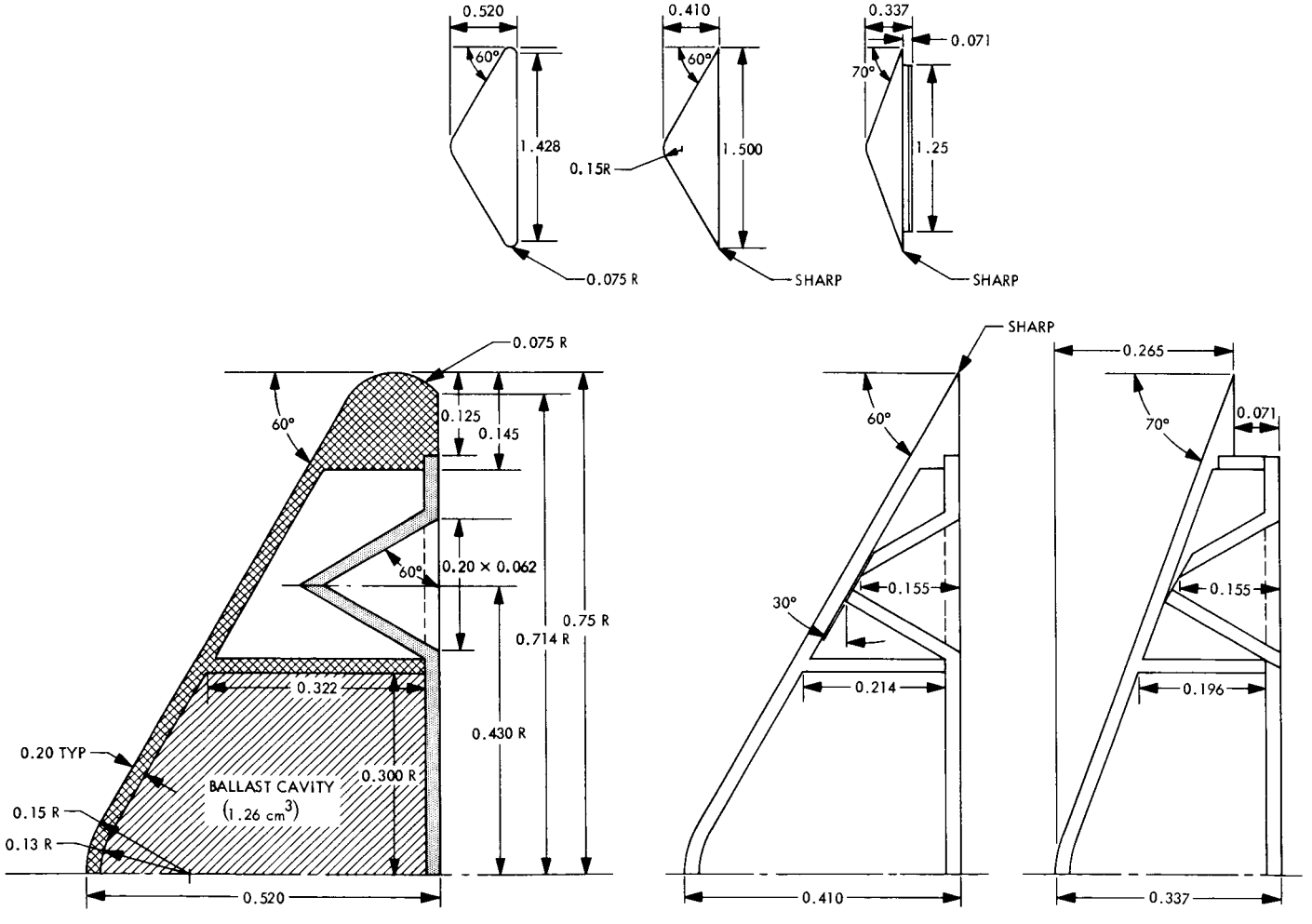

MATERIAL: POLYSTYRENE PLASTIC
BALLAST: TUNGSTEN POWDER

ALL DIMENSIONS IN INCHES UNLESS OTHERWISE SPECIFIED

Fig. 9. Free-flight model designs

that required a sharp blow for disintegration. The weights of two models, one using lead for ballast and the other powdered tungsten, were compared. A sharp-edged cone (1½-in.-diam with a 0.6-in.-diam cylindrical ballast) with a semi-vertex angle of 60 deg weighed 15.8 g using solid lead, and 19.0 g using powdered tungsten. Table 1 summarizes the nominal physical characteristics of the models tested.

Table 1. Nominal model characteristics

Configuration	m, slugs	I, slug-ft^2	d, ft	$(md^2)/I$	$(CG/d)_{nose}$
$M_{60}N_{10}E_{00}$	1.3×10^{-3}	0.32×10^{-6}	0.125	63	0.165
$M_{60}N_{10}E_{05}$	2.0×10^{-3}	0.63×10^{-6}	0.125	49	0.208
$M_{70}N_{10}E_{00}$	1.2×10^{-3}	0.28×10^{-6}	0.125	65	0.133

See nomenclature for definition of symbols.

The cones with semi-vertex angles of 60 and 70 deg do not lend themselves to the pneumatic gun launching device ordinarily used at JPL (Ref. 3). Usually a triangular blade that slips into a slot in the base of the model is attached to the piston shaft of the gun. However, blunt shapes do not have enough length to accommodate a single blade without drastically reducing the ballast volume. The circular launching pad shown in Fig. 10 was used in this experiment. The circular pad supports the model during its acceleration. The location of the two small blades in base slots on either side of the ballast restricts the motion of the model to the pitch plane until the model separates from the blades, the sides of the blades being parallel to the pitch plane. Because the blades are tapered, the model is released when the pad decelerates and then it is free to pitch as the result of aerodynamic forces. This type of support has proved moderately effective for the range of angle of attack (0, 5, 10, and 15 deg) used in this test. Larger blades should provide more launch stability. The launch angles selected for the amplitude studies were pre-established by drilled and tapped holes in the launch pad. The desired launch angle was obtained by rotating the pad about a central pivot to the proper hole combination and inserting two restraining pins. The possible launch angles are limited only to the number of hole combinations provided for in the launch pads.

IV. Data Reduction

The raw data from the free-flight technique consists of motion picture film from which the position of the model with respect to the wind tunnel, and the angle-of-attack history of the model may each be determined as a function of time. The reduction of these measurements to aerodynamic coefficients will be described here briefly. Reference 4 presents an excellent derivation of these data

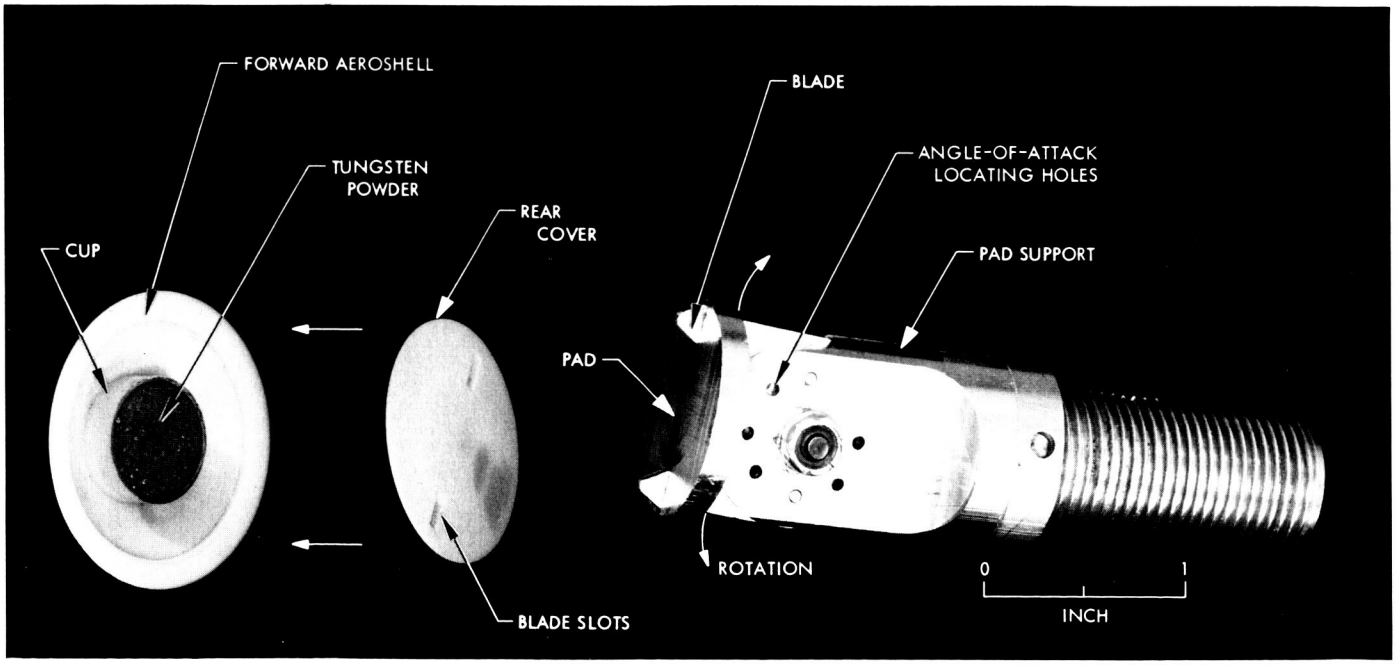

Fig. 10. Typical free-flight model (exploded view) and launch pad

reduction equations, which were applied to the transonic speed regime without change.

A. Drag

Throughout the data reduction, the center of gravity of the model is related to the moving gas media. The distance X appears as the dependent variable in the equation of motion. The equation of motion in the X-direction is

$$-m\ddot{X} = \frac{1}{2}\rho V^2 A C_D \tag{1}$$

from which the drag coefficient is determined. Changing the derivative with respect to time to a distance derivative gives the result

$$C_D = \frac{-2m}{\rho A}\frac{\mathrm{d}(\ln V)}{\mathrm{d}X} \tag{2}$$

A plot representative of $\ln(1 - V_m/V_\infty)$ vs X is shown in Fig. 11. A linear fit through a section of this curve yields, by means of Eq. (2), an effective drag coefficient for that section. Three effective drag coefficients are shown in the figure to indicate the change in drag owing primarily to the change in Mach number, since the effective angle of attack is constant for this flight (Fig. 8). Interestingly, C_D appears to increase slightly, at the first part of the flight, with decreasing Mach number. Near the end of the flight, the slope of the $\ln(1 - V_m/V_\infty)$ curve changes most rapidly, indicating a change of C_D to 1.083 near $M = 0.95$. Careful consideration should be given to oscillation amplitude effects, for they can be significant in data reduction for some shapes. In the case of the blunt shapes tested here, effects of oscillation amplitude were not a significant factor to be considered in reduction of drag, as shown by these transonic test data.

B. Static Stability

The solution to the equation of planar angular motion

$$I\ddot{\theta} = \frac{1}{2}\rho V^2 A\, dC_m + \frac{1}{2}\rho V^2 A\, d\,(C_{m_q} + C_{m_{\dot{\alpha}}})\left(\frac{\dot{\theta}d}{V}\right) \tag{3}$$

(assuming linear aerodynamic coefficients $C_m = C_{m_\alpha}\,\alpha$, $C_L = C_{L_\alpha}\,\alpha$, $C_D = C_{D_0}$) is

$$\theta = \theta_0 e^{\lambda X}\cos\left[\left(\frac{-\rho A d}{2I}C_{m_\alpha} + \lambda^2\right)^{1/2} X\right] \tag{4}$$

where

$$\lambda = \frac{\rho A}{4m}\left[C_{D_0} - C_{L_\alpha} - \frac{md^2}{I}(C_{m_q} + C_{m_{\dot{\alpha}}})\right]$$

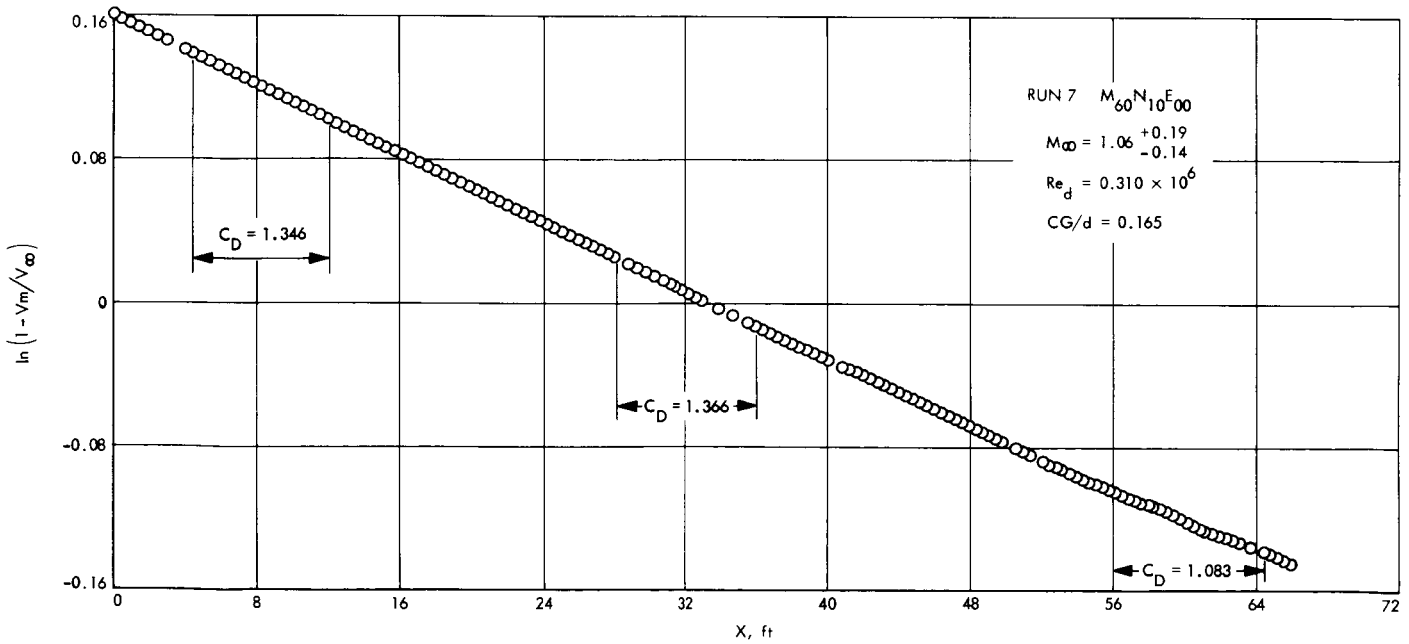

Fig. 11. Plot used for calculation of drag coefficients

The usual assumption is that $(-\rho AD/2I)\, C_{m_\alpha} \gg \lambda^2$ and a resultant effective pitching moment slope is described by

$$(C_{m_\alpha})_{eff} = \frac{-2\, I\Omega^2}{pAd} \tag{5}$$

where Ω is the distance frequency of oscillation. Deviations from a constant value as the oscillation amplitude is varied, are a measure of the nonlinearity of the actual pitching moment. The static stability coefficients presented in this report are effective coefficients calculated from Eq. (5). Because of the relatively low oscillation amplitudes encountered in this experiment and the linearity of the pitching moment slope (Ref. 8) at these amplitudes, methods for determining the coefficients of an assumed nonlinear form developed in Ref. 4 were not used.

C. Dynamic Stability

The dynamic stability coefficients may be obtained from Eq. (4) in terms of the amplitude envelope as

$$(C_{m_q} + C_{m_{\dot\alpha}})\frac{md^2}{I} = \frac{4m}{\rho A}\frac{1}{(X - X_0)} \ln\left(\frac{\theta_x}{\theta_0}\right) + C_{L_\alpha} - C_{D_0} \tag{6}$$

However, Eq. (6) presupposes aerodynamic coefficients whose variations with angle of attack are linear. A more general solution, assuming that the pitching moment is not a linear function of angle of attack during the flight, and lift and drag are of the theoretical form

$$C_L = C_{L_\alpha}\alpha + \mathrm{k}\alpha^3$$

and

$$C_D = C_{D_0} + \mathrm{K}\alpha^2$$

is

$$(C_{m_q} + C_{m_{\dot\alpha}})\frac{md^2}{I} = \frac{4m}{\rho A}\left(\frac{1}{X - X_0}\right)\ln\left(\frac{\theta_x}{\theta_0}\right)R + C_{L_\alpha} + \frac{3}{4}\mathrm{k}\bar\alpha_0^2) - \left(C_{D_0} + \frac{\mathrm{K}\bar\alpha_0^2}{4}\right) \tag{7}$$

where K and k are constants of proportionality to account for nonlinear static coefficients.

The derivation of Eq. (7) may be found in Ref. 4, where the pitching moment correction ratio R has been plotted vs θ_0 for several values of C_{m_α}/r_m. The correction factor is nearly 1 for $\theta_0 = 10$ deg and small values of r_m associated with these blunt bodies. No correction for nonlinear pitching moment was made to the data presented in this report.

The dynamic stability Eqs. (6) and (7) assume that the oscillatory motion of the model will be restricted to one plane normal to the axis of schlieren path. In the case of this investigation, a number of the flights were characterized by motion in both the yaw and pitch planes. Data from those flights only in which the motion was very nearly planar were reduced to aerodynamic coefficients and a procedure was established to determine the total angle of attack for each of the flights. Individual film frames showing the model at peak oscillation amplitude were enlarged and printed. Models exhibiting motion in a vertical plane (perpendicular to the schlieren light path) appear on film as having a flat base while those having motion not restricted to the vertical plane have an elliptic base. The degree of ellipticity in the photographic prints was measured and a corresponding yaw angle ψ computed. This angle was used, in turn, to compute the total angle of attack θ by the equation

$$\tan^2\theta = \tan^2\alpha + \frac{\tan^2\psi}{\cos^2\alpha} \tag{8}$$

The total angle of attack θ was then used to compute $\{C_{m_q} + C_{m_{\dot\alpha}}\}$ by means of Eq. (7), recognizing that the correction of the angle and the assumption of quasi-planar motion may lead to some small error in the final coefficient. The validity of this correction was, however, substantiated by the quality of the test data. Good agreement is shown for flights with varying degrees of yaw, especially those with constant peak amplitude of oscillation.

The applicability of the dynamic stability Eq. (7) was verified with an exact computer solution of the equations of motion. The static stability coefficients, including their dependence on amplitude, and the dynamic stability coefficient reduced from flight data, were entered into the computer program and the resultant motion computed. This motion represented by the computed peak amplitudes[3] is shown in Fig. 12 with the peak amplitudes of run 2 at $M_\infty = 0.84$. The difference between the damping coefficient reduced from flight data and that resulting from the computer solution is only 4%. A similar comparison was performed for run 7, a flight of

[3]Complete test conditions are given in Table 2.

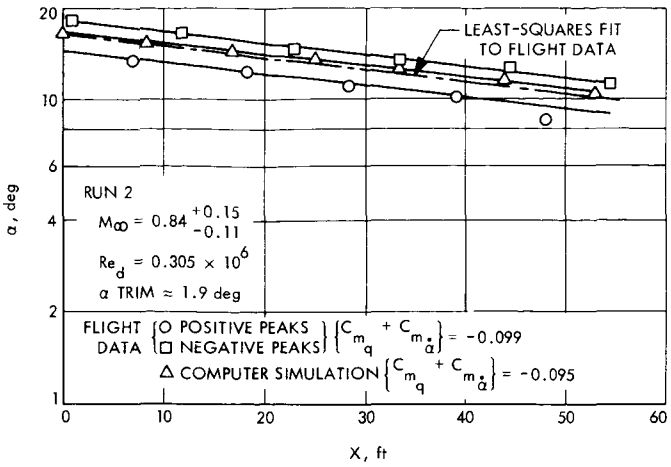

Fig. 12. Typical amplitude plot

constant peak amplitude. The difference between the flight damping coefficient (−0.038) and that of the computer solution was less than 1%. Generally, only one effective dynamic stability coefficient was obtained from a flight, but where amplitude or Mach number effects caused significant changes in the convergence or divergence of the amplitude envelope, the data were segmented and two damping coefficients were obtained. Correlation parameters M and α_0 were also computed for each of these segments.

D. Data Correlation Parameters

The correction terms necessary to account for the nonlinear aerodynamics over an arbitrary number of cycles are based on a mean amplitude for the flight.

This mean amplitude is defined as

$$\bar{\alpha}_0^2 = \frac{2\int_0^X \alpha^2 dX}{X} = \frac{\alpha_X^2 - \alpha_0^2}{2\ln\left(\frac{\alpha_X}{\alpha_0}\right)} \tag{9}$$

when constant decay is assumed to be small in comparison with the oscillation frequency.

Similarly, a mean Mach number M has been used in data presentations because of the large Mach number gradients encountered by a model during its flight.

This mean Mach number is defined as

$$\bar{M} = \frac{\int_0^X M dX}{X} \tag{10}$$

and has been found to agree with M_∞ (within 1%) when the amplitude history of an entire flight was considered. Where it was necessary to separate the flight into segments because of amplitude or Mach effects evident from nonconstant damping, a mean Mach number was calculated by numerical integration (Simpson rule) for each segment.

V. Discussion of Results

The test program was designed primarily to document the dynamic stability of one configuration, $M_{60}N_{10}E_{00}$, in the transonic speed regime when the effects of both oscillation amplitude and Mach number were investigated. Three free-stream Mach numbers—0.95, 1.05, and 1.15—were emphasized. However, data from additional flights were recorded in the range of 0.54 to 2.01. Data obtained from flights of configurations $M_{60}N_{10}E_{05}$ and $M_{70}N_{10}E_{60}$ were desired for comparison with those of the prime configuration. While the majority of flights were made at a nominal Reynolds number of 0.312×10^6 (based on the model diameter of 1.5 in.), two flights were recorded at $Re_d = 0.187 \times 10^6$.

All pertinent information regarding the test conditions and other statistical information of the flights is listed in Table 2. Because of the large range of Mach numbers encountered by a model during a typical flight and the significant changes in aerodynamic coefficients through the transonic regime, the ranges of values resulting for each run are shown for parameters such as M, $\{C_{m_q} + C_{m_{\dot\alpha}}\}$ and C_D. These ranges are indicated by the slash marks shown in the table. Generally only one value of effective dynamic stability coefficient was obtained from a flight; however, where the decay in amplitude varied considerably during the flight, the data were separated into segments and two coefficients were obtained. These changes in dynamic stability during the flight were related to either Mach number or oscillation amplitude effects. The aerodynamic coefficients reduced from data obtained on drag and static and dynamic stability are presented as functions of both Mach number and oscillation amplitude in Figs. 13 through 19.

A. Dynamic Stability

The effect of Mach number on the dynamic stability of the sharp-edged cone ($M_{60}N_{10}E_{00}$) with a half-angle of 60 deg is summarized in Fig. 13 by the solid symbols. Generally, the coefficients are stabilizing at subsonic and supersonic speeds, while decreasing in stability and even

Table 2. Test conditions and data summary

Run	Configuration	M_∞	ΔM	P_t, lb ft^{-2}	T_t, °F	$Re_d \times 10^{-6}$	$\omega d/V \times 10^2$	CG/d	$\bar{\alpha}_0$, deg	$(C_D)_{eff}$	$(C_D)_{range}$	$(C_{m_\alpha})_{eff}$	$\bar{M}$	$\{C_{m_q} + C_{m_{\dot{\alpha}}}\}$	ψ rms, deg
2	$M_{60}N_{10}E_{00}$	0.84	+0.15 −0.11	1186	65.2	0.305	7.38	0.166	13.13	1.110	1.26 / 1.08	−0.156	0.84	−0.099	5
3		1.15	+0.18 −0.15	1091	63.0	0.310	5.76	0.168	11.34	1.369	1.40 / 1.27	−0.135	1.15	−0.034	5
5		0.93	+0.17 −0.13	1125	62.9	0.305	6.93	0.165	10.14 / 7.19	1.240	1.38 / 1.27	−0.154	0.99 / 0.85	−0.037 / −0.182	3
7		1.06	+0.19 −0.14	1109	65.2	0.310	6.21	0.166	13.00	1.319	1.35 / 1.08	−0.137	1.06	−0.038	0
9		1.30	+0.18 −0.17	1096	64.4	0.310	5.30	0.167	11.14	1.410	1.41 / 1.40	−0.130	1.30	−0.093	6
18		1.03	+0.16 −0.13	1122	69.4	0.308	6.44	0.168	10.53	1.323	1.43 / 1.17	−0.146	1.03	−0.077	4
19		1.05	+0.16 −0.05	663	60.8	0.187	4.74	0.165	15.73	1.371	1.46 / 1.09	−0.136	1.05	−0.109	4
20		0.54	+0.12 −0.093	1145	57.6	0.311	9.89	0.168	7.44	1.015		−0.193	0.54	−0.115	3
21		0.69	+0.15 −0.10	1299	58.6	0.307	8.24	0.163	5.97	1.061		−0.155	0.69	−0.139	3
22		0.85	+0.16 −0.11	1165	58.8	0.307	7.40	0.167	6.95	1.110	1.32 / 1.01	−0.157	0.85	−0.055	4
23	$M_{60}N_{10}E_{00}$	1.04	+0.18 −0.14	1094	60.5	0.308	6.22	0.168	11.26	1.346	1.39 / 1.01	−0.141	1.04	+0.005	5
25	$M_{70}N_{10}E_{00}$	0.85	+0.17 −0.12	1167	59.4	0.307	7.30	0.131	10.87 / 7.61	1.185	1.46 / 1.12	−0.135	0.91 / 0.77	+0.041 / −0.099	0
28	$M_{60}N_{10}E_{00}$	1.03	+0.19 −0.13	1091	63.7	0.304	6.59	0.163	8.58	1.326	1.37 / 1.08	−0.157	1.03	−0.011	4
29		0.94	+0.17 −0.12	1126	61.8	0.307	6.75	0.161	6.67 / 5.81	1.208	1.32 / 1.06	−0.148	1.01 / 0.88	+0.011 / −0.137	5
31		1.04	+0.19 −0.14	1111	61.4	0.312	6.38	0.161	11.34	1.339	1.37 / 1.13	−0.150	1.04	−0.011	5
32		0.93	+0.17 −0.13	1124	58.2	0.308	7.00	0.167	12.15	1.120	1.32 / 1.09	−0.160	0.97 / 0.87	−0.037 / −0.355	8
33	$M_{60}N_{10}E_{00}$	1.15	+0.19 −0.15	1088	59.9	0.312	5.98	0.164	10.55	1.378	1.38 / 1.24	−0.138	1.15	−0.056	6

Table 2 (contd)

Run	Configuration	M_∞	ΔM	P_t, lb ft^{-2}	T_t, °F	$Re_d \times 10^{-6}$	$\omega d/V \times 10^2$	CG/d	$\bar{\alpha}_o$, deg	$(C_D)_{eff}$	$(C_D)_{range}$	$(C_{m_\alpha})_{eff}$	$\bar{M}$	$(C_{m_q} + C_{m_{\dot{\alpha}}})$	ψ rms, deg
35	$M_{60}N_{10}E_{05}$	1.03	+0.17 −0.13	1106	64.7	0.307	4.32	0.208	12.27	1.253	1.27 / 1.21	−0.133	1.03	+0.018	0
38	$M_{70}N_{10}E_{00}$	1.15	+0.19 −0.15	1091	62.0	0.311	5.99	0.131	9.53	1.436	1.45 / 1.40	−0.119	1.15	−0.030	2
39	$M_{60}N_{10}E_{05}$	1.15	+0.15 −0.13	1093	62.1	0.311	3.98	0.209	11.48 / 13.06	1.249	1.28 / 1.16	−0.128	1.22 / 1.10	+0.036 / −0.028	0
40	$M_{60}N_{10}E_{00}$	1.06	+0.19 −0.14	1103	61.9	0.311	6.35	0.167	10.72	1.334	1.35 / 1.13	−0.142	1.06	+0.013	4
41	↓	1.04	+0.16 −0.14	1103	59.9	0.311	6.33	0.171	9.13	1.298	1.38 / 0.97	−0.141	1.04	+0.024	6
42		0.93	+0.18 −0.14	1124	58.8	0.307	6.52	0.163	9.43 / 8.66	1.222	1.33 / 1.08	−0.144	0.99 / 0.85	+0.066 / −0.200	4
45		1.06	+0.17 −0.15	1104	61.1	0.311	5.96	0.163	8.48 / 11.06	1.342	1.43 / 1.30	−0.137	1.13 / 0.98	+0.058 / −0.094	6
46		1.30	+0.17 −0.16	1096	65.2	0.310	5.14	0.162	9.62	1.362	1.41 / 1.36	−0.129	1.30	−0.051	6
48	$M_{60}N_{10}E_{00}$	2.01	+0.23 −0.21	1388	77.9	0.309	4.07	0.165	5.02	1.494		−0.139	2.01	−0.247	0
49	$M_{70}N_{10}E_{00}$	1.30	+0.21 −0.16	1104	67.9	0.310	5.70	0.133	9.09	1.487	1.55 / 1.45	−0.125	1.30	+0.024	0
50	$M_{60}N_{10}E_{05}$	1.30	+0.16 −0.14	1099	66.6	0.309	3.71	0.208	14.43	1.313	1.34 / 1.26	−0.126	1.30	−0.071	5
51	$M_{60}N_{10}E_{00}$	1.03	+0.17 −0.13	663	61.4	0.186	4.65	0.163	15.02 / 13.30	1.368 / 1.280	1.368 / 1.28	−0.135 / −0.144	1.03	−0.044	2
53	↓	0.93	+0.19 −0.13	1130	65.2	0.304	6.48	0.164	14.70 / 12.81	1.246	1.44 / 1.16	−0.145	0.94 / 0.85	−0.034 / −0.158	4
56		1.04	+0.21 −0.14	1116	63.9	0.312	6.22	0.166	9.01	1.344	1.38 / 1.18	−0.147	1.04	−0.016	4
57	$M_{60}N_{10}E_{00}$	1.15	+0.18 −0.15	1100	64.6	0.312	5.60	0.163	11.71	1.383	1.44 / 1.32	−0.133	1.15	−0.020	4
59	$M_{60}N_{10}E_{05}$	1.05	+0.18 −0.15	1115	64.1	0.312	4.36	0.210	16.34	1.226	1.27 / 1.23	−0.129	1.05	−0.023	3
61	$M_{60}N_{10}E_{00}$	1.15	+0.17 −0.13	1088	61.2	0.311	5.65	0.165	8.13 / 10.97	1.402	1.45 / 1.38	−0.135	1.25 / 1.09	+0.085 / −0.032	4

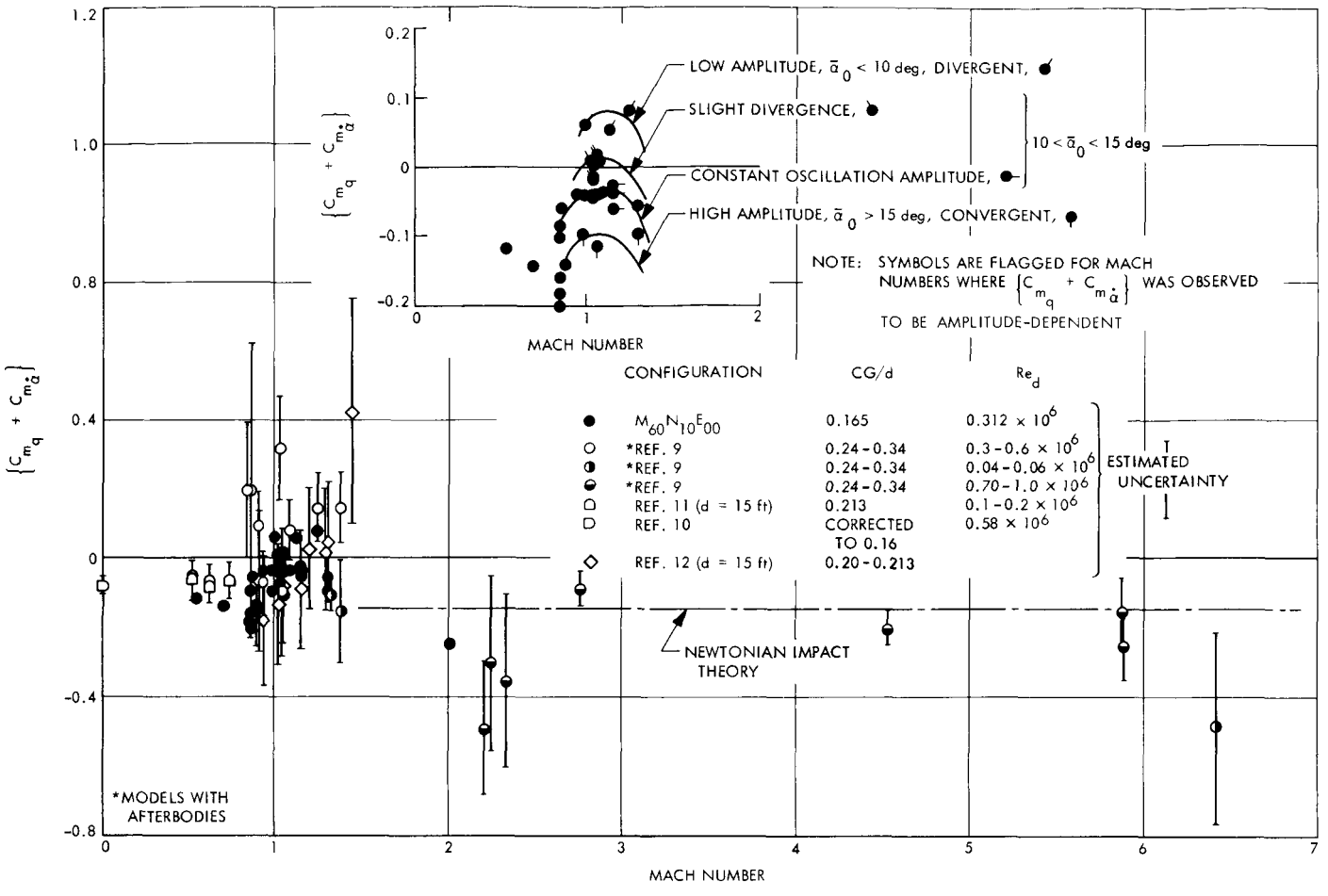

Fig. 13. Effect of Mach number on free-flight dynamic stability of the sharp-edged 60-deg cone

destabilizing (positive) at transonic speeds. The magnitude of this transonic destabilizing tendency is not so severe as has been suggested by other test data (Ref. 9) and the relatively close grouping of the data in the transonic regime indicates good repeatability.

In detail, the single definite supersonic data point at $M = 2.01$ suggests a stability level in excess of that computed by Newtonian impact theory, a conclusion supported to some extent by the data of Ref. 9.[a] Little more can be inferred from these data about the specific level of stability for this configuration at supersonic speeds until more definitive experimental evidence is available. The experimental results for the round-edged 60-deg-half-angle cone indicate stability levels similar to these data and will be discussed later.

[a]Data of Refs. 9, 10, 11, and 12 have been divided by 2 so that they might agree with JPL data reduction relating $(C_{m_q} + C_{m_{\dot{\alpha}}})$ to $\theta d/V$ rather than to $\theta d/2V$.

Although the experimental program was directed toward the definition of transonic dynamic stability for these shapes, a few subsonic data points were obtained and are shown in Fig. 13. As models that had been launched at an approximate free stream Mach number of 0.95 slowed to subsonic speed ($M \sim 0.9$), the decay in oscillation amplitude increased greatly. As previously stated, these runs were reduced in two segments. The coefficients resulting from the second half of the flights at $M_\infty = 0.95$, and flights at $M_\infty = 0.85$, result in a wide range of dynamic damping, $\{C_{m_q} + C_{m_{\dot{\alpha}}}\}$, shown in the figure at $M = 0.85$. This area appears to be a transition region between the transonic and subsonic regimes where the dynamic stability is increasing rapidly with decreasing Mach number. Further decreases in Mach number result in coefficients that are less favorable. The one, low, subsonic data point near $M = 0$ (Ref. 10) obtained in a vertical wind tunnel has been corrected for the forward center-of-gravity location, CG = $0.167d$, indicated by the technique outlined in the reference. Dynamic sta-

bility is apparently more favorable for a forward shift in center of gravity at subsonic speeds. The data of Ref. 11 show slightly less stability than the two subsonic coefficients of this experiment. However, these less favorable coefficients may simply be the result of the relatively aft center-of-gravity location.

During the course of reducing the motion history data to coefficient form, a pattern developed in the transonic data which indicated that the coefficients might be categorized by the type of motion history observed. The majority of these flights, or a part of them, occurred either at constant oscillation amplitude or with slightly divergent envelopes. The histories were apparently convergent to this type of motion because few flights resulted in coefficients that were not of these two types. However, a few models launched at low amplitudes ($\bar{\alpha}_0 < 10$ deg) were found to have divergent motion while those launched at the highest amplitudes ($\bar{\alpha}_0 > 15$ deg) were strongly convergent. The results showing distinct amplitude effect on dynamic stability of these shapes help to explain the small range of amplitudes for which data were recorded. Because of the scale used in Fig. 13, these effects are not clearly defined and the data have been replotted on an expanded scale in the inset. The four distinct types of observed motion related to amplitude effects are evident and have been further identified by flagged symbols and fairings. In detail, strong divergence may be observed for flights in which the oscillation envelope of the model was less than 10 deg ($\bar{\alpha}_0 < 10$ deg) and convergence observed for envelopes that were more than 15 deg ($\bar{\alpha}_0 > 15$ deg). As described, two types of motion were observed in the amplitude range of 10 to 15 deg: (1) constant oscillation amplitude, and (2) slight divergence resulting in slightly positive coefficients. These data and their dependence on oscillation amplitude are crossplotted in a figure on page 19.

Transonic data are also shown in Fig. 13 that were obtained in a ballistic range (Ref. 9) and from full scale (15-ft-diam conical spacecraft) flight tests in the atmosphere of the earth (Ref. 11). The coefficients from Ref. 9 are for the most part destabilizing (positive) in the transonic regime while the data from Ref. 11, with the exception of one data point, are very similar to the data of this experiment. The flight test data may be difficult to pick out from the concentration of transonic coefficients. It has been suggested by Whitlock et al. (Ref. 12) and Sammonds (Ref. 13) that extremely destabilizing coefficients are the result both of aft center-of-gravity locations and of low oscillation amplitudes. Although at transonic speeds dynamic stability seems to decrease with decreasing oscillation amplitude, it is difficult when considering all available data to concur with this hypothesis without more conclusive evidence. An experimental program that specifically separates the effects of center-of-gravity location from those of oscillation amplitude is needed to clarify such questions about the effects of center of gravity.

The dynamic stability of the round-edged 60-deg-half-angle cone ($M_{60}\,N_{10}\,E_{05}$) and the sharp-edged 70-deg cone ($M_{70}\,N_{10}\,E_{00}$) is shown in Fig. 14. The data for these configurations are not sufficient to specify their transonic dynamic stability characteristics with the detail shown for the sharp-edged 60-deg cone (Fig. 13). However, the general levels and range of the coefficients are remarkably similar to those shown for the basic configuration $M_{60}\,N_{10}\,E_{00}$. As in Fig. 13, transonic data from Ref. 9 are shown for a configuration similar to $M_{60}\,N_{10}\,E_{05}$ but with a more rearward center-of-gravity location. These data suggest less favorable transonic dynamic stability and even trends toward unfavorable stability at subsonic speeds. In contrast, the subsonic coefficient for $M_{70}\,N_{10}\,E_{00}$, a configuration that has transonic dynamic stability similar to that of $M_{60}N_{10}E_{00}$ (Fig. 13) and $M_{60}N_{10}E_{05}$, is stabilizing.

No supersonic flights at $M_\infty > 2.01$ were made with these configurations during this experimental program. However, some unpublished results[5] were available for the $M_{60}\,N_{10}\,E_{05}$ configuration from an experimental program conducted in the JPL 20-in. supersonic wind tunnel for the development of planar launching techniques in connection with this transonic test. The coefficients for these data have been plotted in Fig. 14 (solid flagged symbols). A stabilizing coefficient of approximately -0.023 was obtained, which becomes less negative with decreasing Mach number and fairs well to the transonic level of dynamic stability as shown by the solid curve. Because of the basic emphasis of the test and of limited time, less than half the models were measured for physical characteristics. Physical properties for nominally identical models, predominantly 60-deg round-edged models with and without afterbodies, varied about 11%, which may account for some of the data scatter at the five test Mach numbers. These conditions are the reason that the data have not been formally published. However, because of the relatively good definition of the supersonic dynamic stability for $M_{60}\,N_{10}\,E_{05}$, the inclusion of these data in this report seemed important.

[5]Internal communication by R. Prislin, JPL, October 1966.

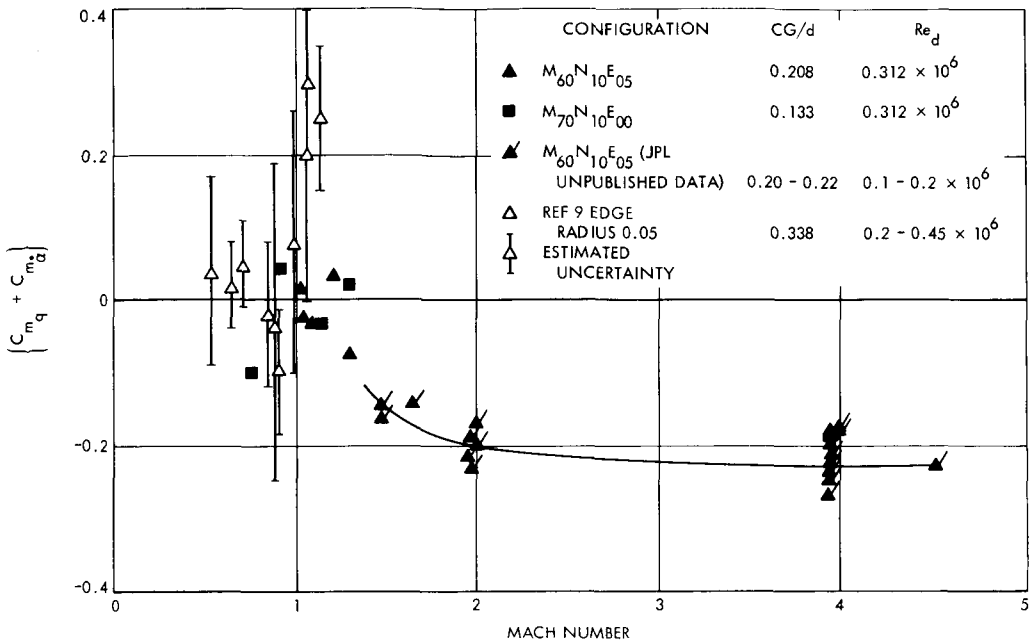

Fig. 14. Effect of Mach number on free-flight dynamic stability of the round-edged 60- and 70-deg cone

Amplitude effects on dynamic stability previously mentioned in reference to Fig. 13 are shown in Fig. 15 for the basic configuration $M_{60}N_{10}E_{00}$ at three transonic Mach numbers. The dynamic stability coefficient $\{C_{m_q} + C_{m_{\dot{\alpha}}}\}$ is for the most part destabilizing at amplitudes of less than 10 deg and becomes more favorable with increasing oscillation amplitude. More than half of these data were recorded in the amplitude range of 10 to 15 deg. Dynamic stability at high amplitude ($\bar{\alpha}_0 > 15$ deg) remains to be defined. Obtaining these data would probably pose no problems. Obtaining data at low amplitudes may be another matter, since oscillation envelopes were observed to diverge rapidly to the amplitudes shown. The physical parameters (i.e., mass, moment of inertia, and diameter) of free-flight models might be tailored to minimize low amplitude divergence. However, the need for low amplitude data has not been demonstrated, since the oscillation envelope of an entry configuration may only diverge, when using the data of this report in computer motion analysis, to amplitudes at which the motion becomes damped.

The dynamic stability coefficient presented in this report is one that is effective over several oscillation cycles and, therefore, is not immediately useful for computer studies of entry motion, which commonly require a coefficient related functionally to a local angle of attack. The local coefficient can not be obtained directly from the experimental data but its functional dependence on oscillation amplitude or Mach number must be hypothesized and then this equation integrated to obtain an effective coefficient that it is hoped will depict the character of the experimental motion history data. Only the following equality[a] must be preserved:

$$(C_{m_q} + C_{m_{\dot{\alpha}}})_{eff} \int_{-(\alpha_0-\delta\alpha)}^{+\alpha_0} \alpha' \, d\alpha = \int_{-(\alpha_0-\delta\alpha)}^{+\alpha_0} (C_{m_q} + C_{m_{\dot{\alpha}}})_{local} \, \alpha' \, d\alpha \tag{11}$$

Therefore, the local dynamic stability coefficient, which appears on the right side of Eq. (11), could be a function of any angle-of-attack variable—α, α', $\bar{\alpha}_0$, etc. This makes the choice of the functional form of the local coefficient difficult. Proof that the local coefficient satisfies the experimental data must be made by computer simulation of the motion history.

The method of obtaining a local dynamic stability coefficient is further described by the following example.

[a]This equation is presented in Ref. 14 in terms of θ rather than α. The angle of attack α has been used here with the assumption that α and θ are the same for these models undergoing acceleration due to drag of two orders of magnitude greater than the gravitational acceleration. The use of α also follows with the practice of presenting amplitude effects on $(C_{m_q} + C_{m_{\dot{\alpha}}})$ in terms of $\bar{\alpha}_0$.

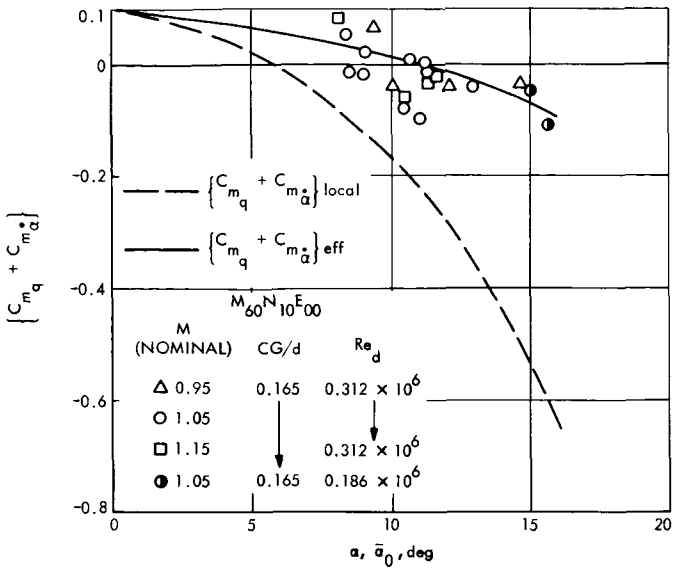

Fig. 15. Effect of oscillation amplitude on dynamic stability

The local coefficient representing the data of Fig. 15 may be hypothesized to be of the form

$$(C_{m_q} + C_{m_{\dot{\alpha}}})_{local} = a + b\alpha + c\alpha^2 + d\alpha^3 \tag{12}$$

and the solution for the effective coefficient by Eq. (11), assuming a linear pitching moment and small decay, is

$$(C_{m_q} + C_{m_{\dot{\alpha}}})_{eff} = a + \frac{4b}{3\pi}|\alpha_0| + \frac{c\alpha_0^2}{4} + \frac{8d}{15\pi}|\alpha_0|^3 \tag{13}$$

where a, b, c, and d are the same polynomial coefficients in both Eqs. (12) and (13). These coefficients were obtained from the curve to the *effective* data (Eq. 13) and then used to determine the character of the *local* curve.

Figure 15 presents both the visual effective curve fit (cubic) and the corresponding local dynamic stability curve. The change in the local curve is attenuated with increasing amplitude when converted to the effective curve. A more detailed explanation of the conversion of the local to the effective coefficient is presented in Ref. 14 with a discussion of the extreme sensitivity of the local coefficient to apparently insignificant changes in the curve fit to a set of effective data. The possible dependence of the local coefficient on α', α_0, and other parameters is also discussed in the reference. The local curve shown in Fig. 15 is preliminary and may change appreciably with more knowledge of the effects of high and low amplitude on the effective dynamic stability coefficient, and the probable effects of scaling parameters.

Sometimes a simple hypothesis may be used to explain amplitude effects. For example, dynamic stability tests of 10-deg-half-angle cones have disclosed that separation on the lee side of the cone at amplitudes near the cone half-angle coincides with increases in dynamic stability. This explanation does not apply to the 60-deg-half-angle cone. A brief examination of separation effects (Ref. 8) has not disclosed any amplitude dependence. Flow separation at the maximum diameter of the model is fixed for the sharp-edged model and is also fixed at the forward part of the round-edged model radius for the range of angle of attack investigated in this experiment. A rigorous analysis of the flow field and model scaling parameters will be necessary before any conclusions about the cause of these amplitude effects can be made. Model scaling parameters were not investigated in this experiment.

B. Drag and Static Stability

Free-flight drag and static stability are presented in Figs. 16–19. The drag data are shown in Figs. 16 and 17 while the static stability data are shown in Figs. 18 and 19. These data are a by-product of the dynamic stability investigation. However, static data are necessary for the reduction of the dynamic damping data to aerodynamic coefficients, and these free-flight data are significant because they are free from support interference. Interference effects have been known to invalidate test data for these shapes in the transonic regime.

The drag rise curve (Fig. 16) was obtained by plotting the effective drag coefficient for each flight. The drag coefficient C_D was computed using the slope of a linear least-squares curve fit to the (ln V) data in Eq. (2). The data for the three configurations tested are consistent

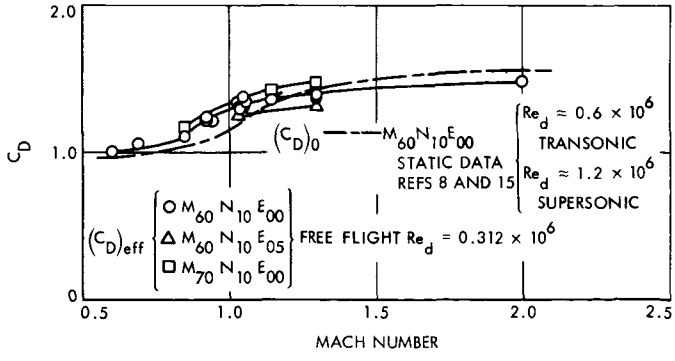

Fig. 16. Effect of Mach number on free-flight drag

with each other and show good repeatability in the transonic regime. The one supersonic data point at $M = 2.0$ where $C_D = 1.49$ is in excellent agreement with the value of 1.50 quoted in Ref. 9. The static drag curve (Refs. 8 and 15) for configuration $M_{60}N_{10}E_{00}$ at $\alpha = 0$ deg is also shown for a general comparison of sting-supported data with those obtained using the free-flight technique. The two curves do not agree in the transonic drag rise part and the cause is not immediately apparent. The natural log plot (Fig. 11) used to compute the free-flight drag also shows this same type of delay in transonic drag drop. As a further check on the free-flight drag, detailed drag vs Mach number histories were generated from raw distance vs time data of runs 7 and 53. The results (not shown) indicated a drag curve similar to that of the effective drag rise curve shown here. Since the variation of free-flight drag with Mach number appears to be genuine, additional work is advised to investigate possible sting interference in the static data and acceleration effects that may be present in the free-flight drag coefficients.

The effect of oscillation amplitude on drag coefficient C_D is shown in Fig. 17. The data for primary configuration $M_{60}N_{10}E_{00}$ are apparently independent of amplitude for the test amplitude range. This result was expected, since a similar independence of amplitude for this range was observed in the data of Ref. 8. Sufficient data for the other configurations were not recorded to define amplitude effects on C_D; however, the trends for all three configurations should be similar, with distinct levels registered for each.

The dependence of the static stability on Mach number is shown in Fig. 18. The configurations tested are all

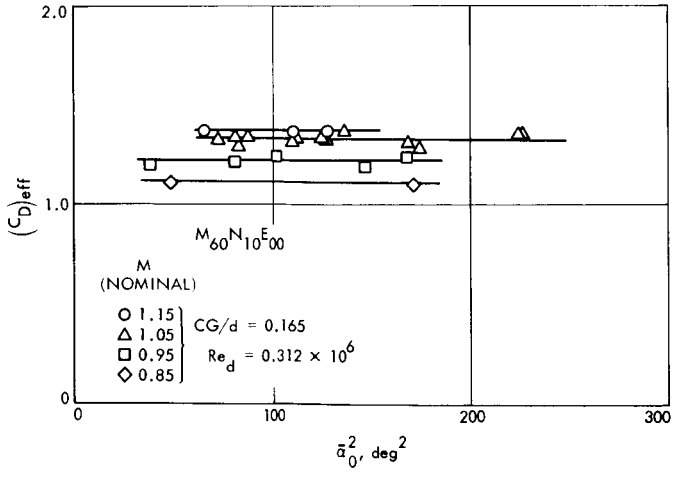

Fig. 17. Effect of oscillation amplitude on free-flight drag

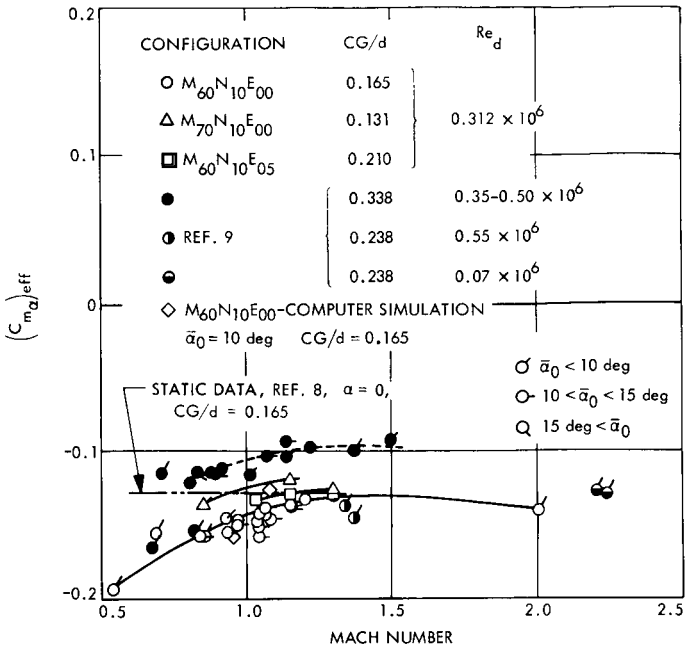

Fig. 18. Effect of Mach number on static stability

statically stable for the test amplitude range, with this static stability increasing with decreasing Mach number. The sharp-edged model is more statically stable than the other configurations. However, the effects of configuration and center of gravity were not investigated and, therefore, are not immediately separable. Data from other investigations have been plotted for the purpose of comparison. The center of gravity of the models of Ref. 9 was significantly further aft of the model nose than those of the other models for which data are shown. This rearward center of gravity location was the result of an afterbody extension designed to move the center of gravity aft and increase the mass moments of inertia and, in turn, improve the quality of dynamic damping data obtained in the ballistic range. Since the static stability is expected to decrease with a rearward displacement of the center of gravity, the data of Ref. 9 (60-deg sharp-edged cone) are consistent with JPL configuration $M_{60}N_{10}E_{00}$, and the data shown for $M_{60}N_{10}E_{05}$ and $M_{70}N_{10}E_{00}$ may be influenced by differences in configuration.

The pitching moment coefficient C_{m_α} obtained from static tests (Ref. 8) is shown for the purpose of comparison by the dashed curve for configuration $M_{60}N_{10}E_{00}$. Center-of-pressure data from the same reference were also used in a computer simulation of the model motion history. The distance oscillation frequency was then used to compute, by the methods described in this report, an effective C_{m_α}. Two coefficients were computed in this

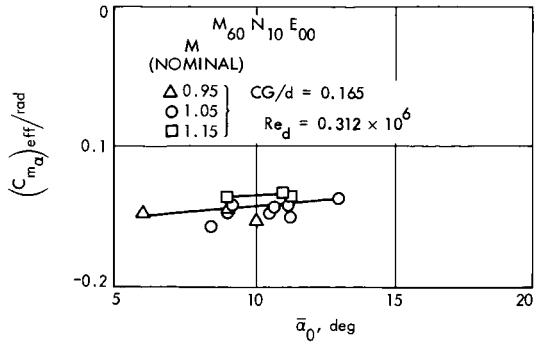

Fig. 19. Effect of oscillation amplitude on static stability

manner and are shown to bracket the data for $M_{60}N_{10}E_{00}$ in the figure.

Free-flight static stability data are correlated with $\bar{\alpha}_0$ in Fig. 19. Sufficient data were available to define oscillation amplitude effects on static stability for configuration $M_{60}N_{10}E_{00}$. Trends of slightly increasing stability with decreasing amplitude are shown for the three basic transonic test Mach numbers 0.95, 1.05, and 1.15 within approximately a 7% spread. Similarly, experimental data of Ref. 8 show increasing static stability margin with decreasing amplitude.

C. Flow Visualization

The photographic data obtained in this experiment not only provide the quantitative results to describe the model time–motion history, but they also give an excellent documentation of the flow field. A continuous motion history of approximately 300 frames for time increments as small as 0.0002 s is available for study for each flight. This information could be used to answer questions prompted by this investigation, in particular, those related to the mechanisms of transonic instability.

A sequence of motion picture frames, each with a black dot providing a fixed point of reference, has been assembled in Fig. 20 to show the primary developments of the flow field as the model traverses the transonic Mach number range. The pictures, taken from run 5 where the free stream Mach number was 0.93, have been identified by frame number and a corresponding Mach number of the model relative to the flow. The range of Mach numbers encountered by the model in the sequence was 1.04 to 0.87. The time between frames is 0.0002 s.

The frames were selected to illustrate some of the significant changes in the flow field observed while these data were viewed as a motion picture sequence. Frame 50 shows a typical picture of the flow about these shapes at transonic Mach numbers. The bow shock wave is detached and a wake of increasing and then decreasing downstream diameter is observed, with the usual recompression wake shock. As the Mach number decreases in succeeding frames, the bow shock wave becomes less distinct and further detached from the model. Without ever actually disappearing, the bow wave disengages from the relative motion of the model at $M = 1.0$. It then travels upstream or downstream with respect to the wind tunnel at the local speed of sound, thereby assuming the character of an acoustic wave. At the same time, the wake becomes less convergent. The wake recompression shock adjusts to these changes by becoming almost perpendicular to the direction of the flow. Dramatic transients in the wake are revealed in frames 170 through 240 in which the recompression shock becomes less distinct and the model actually passes through the remaining weak disturbances at $M = 0.879$ (frame 220).

Much of the interesting oscillatory nature of the wake is lost by fixing the motion picture history in still-photographs, yet the flow detail necessary to investigate the mechanisms of transonic dynamic stability for many shapes is clearly indicated. Since the flow about the forebody is without the direct influence of the bow wave for much of the flight, and transient separation on the model edge has not been observed, the wake should be examined for possible influences on the dynamic stability of these shapes. An inquiry of this nature is a sizable task in itself and will not be considered here.

VI. Application of Experimental Data

This section is devoted to a discussion of the use of experimental test data to simulate through computer studies the angle-of-attack envelopes of a 60-deg-half-angle spherically blunted cone vehicle during entry into an assumed Martian atmosphere.

When computing the motion history of an entry capsule with a six-degree-of-freedom program, the dynamic stability coefficient must be specified both as a function of Mach number and of local angle of attack. The local coefficient can be obtained by previously described techniques in which the nature of the local coefficient is hypothesized. In view of the uncertainties present in this method, an alternate and more practical method for preliminary motion studies was used here. A local coefficient both planar and nonplanar must be derived eventually for use in more comprehensive motion studies because of time and expense imposed by the following iterative procedure.

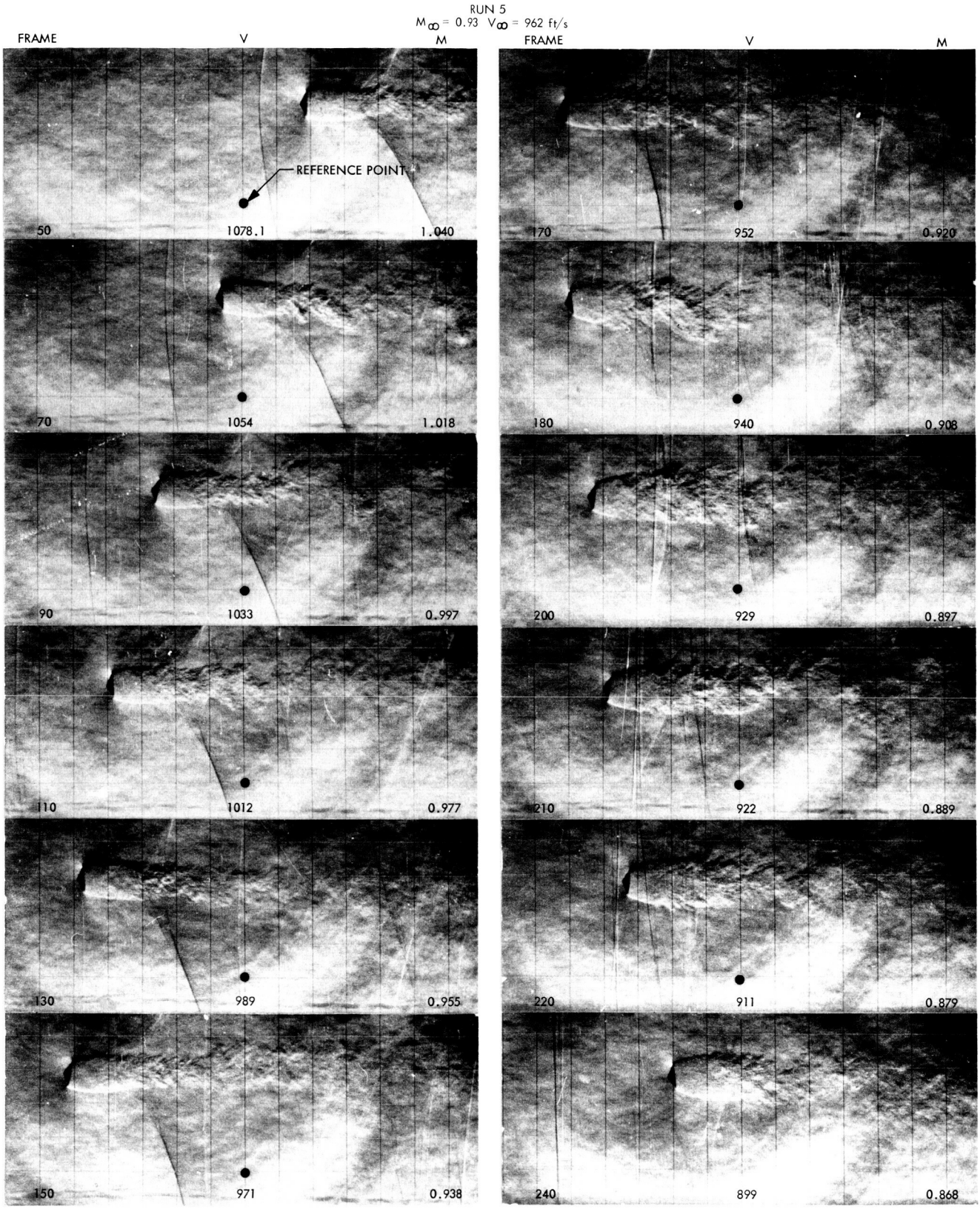

Fig. 20. Key flow field events

The alternate method used here is one in which the oscillation envelope and corresponding dynamic stability history are obtained by an iterative technique. An angle-of-attack history, which has been computed or assumed, is used to synthesize a $\{C_{m_q}+C_{m_{\dot{\alpha}}}\}_{eff}$ history compatible with $\bar{\alpha}_0$ and Mach number using experimental amplitude-dependent data. This dynamic stability curve should be a function of Mach number only. A new trajectory is computed using the previously synthesized curve, and from this trajectory a new dynamic stability history as a function of Mach number is determined as before. The iteration process is continued until the amplitude solution converges with the presupposed dynamic stability history. This $\{C_{m_q}+C_{m_{\dot{\alpha}}}\}$ vs Mach number curve represents the solution for the particular initial conditions chosen for the trajectory, the entry capsule, and the atmosphere. Further iterations are necessary for changes in these conditions.

The vehicle characteristics and key trajectory parameters used in the following computer simulations are given in Table 3. The trajectories used a 20-mbar surface-pressure atmosphere intended to represent the upper limit of Martian atmospheres. The static stability coefficients used in the computer program were drawn from Refs. 15 and 8, and unpublished data from experiments conducted at the NASA Langley Research Center.

Figure 21 presents the vehicle angle-of-attack envelope vs Mach number for the Mars entry trajectories. The corresponding Mach-number-dependent dynamic stability curves are shown in Fig. 22. The dashed curve (Fig. 22)

Table 3. Initial conditions for Mars entry

Parameter	Entry condition
Trajectory	
V, ft s^{-1}	23,000
γ_E, deg	50 at 0.8 × 10^6 ft
α_E, deg	50
Capsule	
m, slugs	5.815
d, ft	6.5
X_{CG}/d	0.19
I_X, slug-ft^2	13.37
I_Y, slug-ft^2	8.03
m/C_DA, slugs ft^{-2}	0.117
Atmosphere	
T_0, °F	35
ρ_0, slugs ft^{-3}	5.3 × 10^{-3}
P_0, mbar	20
g, ft s^{-2}	12.3
β, ft^{-1}	2.12 × 10^{-5}

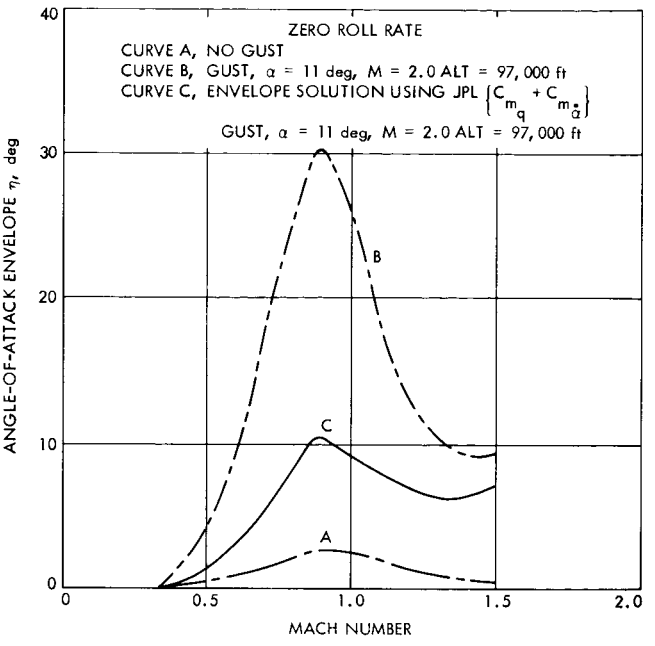

Fig. 21. Low speed angle-of-attack envelopes for Mars entry

was originally a conservative (unfavorable) estimate of the dynamic stability of the 60-deg-half-angle cone configuration based on Newtonian theory and some of the experimental data presented in this report. No oscillation amplitude dependence was assumed in the dashed curve.

Curve A in Fig. 21 represents the envelope for the terminal part of the entry trajectory, including the transonic–subsonic regimes. Because of the negative stability coefficient (Fig. 22, dashed curve), the vehicle is well damped and the angle of the envelope is less than 1 deg above an altitude of 97,000 ft at $M=2$. Divergence to $\eta = 2.7$ deg may be observed in the transonic regime and is the result of the destabilizing coefficient described for these speeds. Even after undergoing such a large change in the dynamic stability coefficient, the vehicle angle-of-attack envelope cannot be judged critical in the sense of tumbling. The envelope is shown only for $M < 1.5$; it is rather uninteresting and well damped at supersonic and hypersonic speeds.

To amplify the transonic divergence a step function gust was introduced in curve A (Fig. 21) at $M=2$, which resulted in an angle of attack of approximately 11 deg. The resultant angle-of-attack envelope (with the dashed curve used for $\overline{C_{m_q}}$ in Fig. 22) is shown in Fig. 21, curve B. The envelope slightly exceeded 30 deg at $M = 0.8$. With the use of this envelope and the pre-

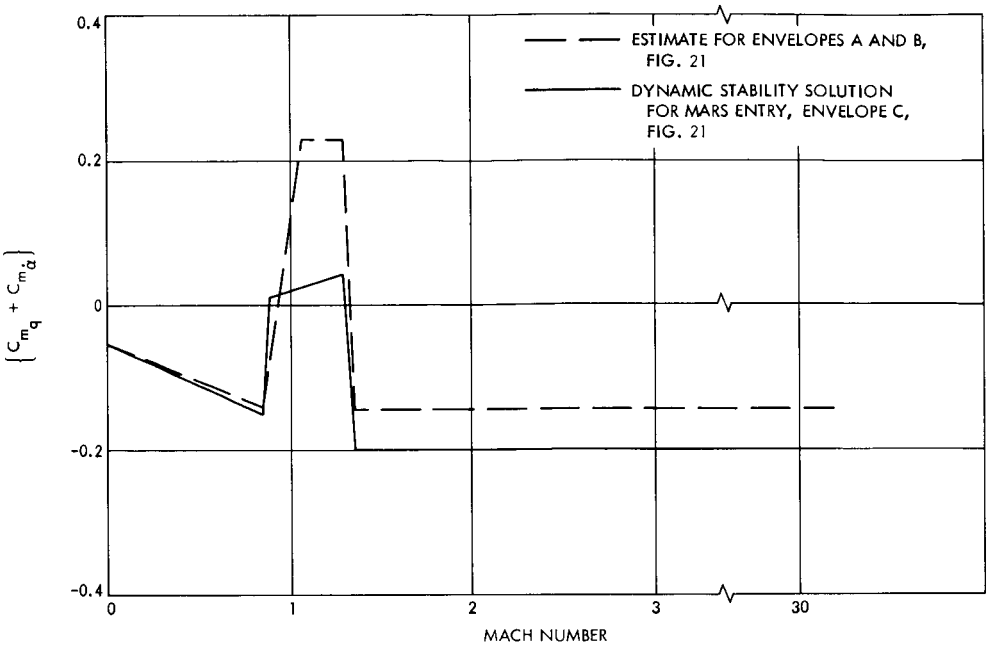

Fig. 22. Variations of the dynamic stability coefficient

viously described iteration process, a solution based on the amplitude-dependent damping data presented in this report was found for η and $\overline{C_{m_q}}$ as a function of Mach number. The result for the envelope is shown in curve C in Fig. 21. No alarming transonic divergence results from the dynamic stability solution shown in Fig. 22 (solid curve).

The data of this experiment have only begun to give insight into the transonic dynamic stability characteristics of the blunt-cone entry shape. Further experimental work must be completed before the local damping coefficient for these configurations can be derived; and in doing so, it is particularly important to consider the possible difference of the dynamic damping data for spinning and nonspinning entry capsules.

Spinning vehicles, whether spun inadvertently or intentionally, are of interest because computer studies (Ref. 16) have shown a serious roll-related angle-of-attack divergence for a 60-deg cone, a phenomenon apparently related to vehicle characteristics and entry conditions. The divergence occurred near the terminal part of the trajectory (subsonic–transonic regimes) where experimental dynamic stability coefficients have been, more often than not, accompanied by large uncertainties. Accurate experimental verification of the spin-induced divergence and better understanding of the transonic dynamic damping characteristics of these shapes in the spinning mode would be helpful in removing some of the uncertainties in the prediction of the angle-of-attack envelope of an actual entry vehicle.

VII. Summary of Results

A parametric investigation of the dynamic stability characteristics of one 70-deg-half-angle cone and two 60-deg-half-angle cones has been conducted at transonic speeds. The parameters considered were primarily Mach number and oscillation amplitude. The following may be concluded from the test results and computer studies performed, in which test data were used to determine the oscillation envelope history of a nominal entry capsule passing through the suspected upper limit of possible Martian atmospheres.

(1) The 60- and 70-deg-half-angle cones do indeed exhibit less dynamic stability in the transonic speed regime compared with the stabilizing values of the coefficients at subsonic and supersonic speeds. However, this destabilizing tendency was oscillation-amplitude-dependent and occurred generally for flights where $\bar{\alpha}_0 < 10$ deg. Constant oscillation amplitudes and slightly divergent envelopes were observed for the amplitude range $10 < \bar{\alpha}_0 < 15$ deg and convergent envelopes for $\bar{\alpha}_0 > 15$ deg. These results may give direction to future investigations which would, it is hoped, include a detailed look at one configuration and scaling parameters such as center-of-gravity location, dimensionless

frequency, and Reynolds number. Spin should also be investigated. Center of gravity would appear to be an important parameter, especially since Sammonds (Ref. 13) has suggested that the more rearward center-of-gravity positions for ballistic range data (Ref. 9) account for a more destabilizing coefficient than those shown for this experiment. Any investigation should be restricted to the use of free-flight techniques (wind tunnel, ballistic range, or full scale flight tests) to ensure that the data are not influenced by a support. Any investigations of sting support interference on dynamic stability should be complemented by a free-flight program. Finally, the possibility of differences if any between data obtained from flights of both planar or nonplanar motion should be investigated. The data of Refs. 9, 10, 11, and 12, and of this experiment, were obtained in somewhat different test environments and constraints; therefore meaningful direct comparison beyond that presented in this report is not possible with the information available.

(2) Free-flight motion data also provide drag and static stability data as a by-product. These static coefficients obtained from free-flight data are in good agreement with the sting supported data (Ref. 8) at subsonic speeds and ballistic range data (Ref. 9) at $M \sim 2$. The transonic drag rise, however, begins at a lower Mach number than the static sting supported data. Before attributing these differences to model acceleration effects alone, the possibility of sting support interference influencing static data, Reynolds number effects, and tunnel blockage should be examined. The drag sensitivity to oscillation was not discernible for the range of amplitude investigated (approximately 0 to 15 deg). Pitching moment slope data show all the configurations tested to be statically stable and these coefficients appear to be consistent within themselves and with other test data. However, the center of gravity must be deliberately varied before its effects and those of configuration can be separated. The coefficient C_{m_α} is shown to be more stabilizing (negative) with decreasing Mach number, and more data are needed in the subsonic regime to better define this trend.

(3) The free-flight technique has been successfully applied to the conditions existing in a slotted wall transonic wind tunnel with certain advantages over other testing techniques. Model characteristics may be optimized to emphasize the character of the experimental data while initial flight conditions such as angle of attack, roll, and yaw are controlled. These advantages are further amplified by the significant number of motion picture data frames recorded (approximately 300/flight) from which both the model angular motion and transients flow field character can be obtained. A biplanar mirror system that has been developed for a conventional supersonic wind tunnel (Ref. 5) would extend the present capability to the study of nonplanar motion exhibited by spinning entry capsule shapes. A comparison of planar and nonplanar motion histories under identical test conditions would then be practical.

(4) The angular motions of a nonspinning entry capsule have been studied on a preliminary basis with the use of a six-degree-of-freedom program. No alarming motions (i.e., tumbling or large oscillation envelopes) were observed in the transonic regime even under a severe gust-induced angle-of-attack change. Much work remains to be done before a damping coefficient based on the local angle of attack can be synthesized for more flexible computer analysis. Since recent computer studies (Ref. 16) have indicated severe transonic–subsonic envelope divergence for certain capsule spin rates it is important that the local coefficient be derived for spinning bodies as well as for those with angular motion restricted to one plane.

Nomenclature

A reference area for model, $\pi d^2/4$

CG center of gravity, distance to center of gravity from physical model nose

C_D drag coefficient, drag force/$q_\infty A$; C_{D_0} is the drag coefficient at $\alpha = 0$

C_L lift coefficient, lift force/qA; C_{L_α} is the lift coefficient slope per radian

C_m pitching moment coefficient, pitching moment/$q_\infty Ad$; $C_{m_{\dot\alpha}}$ is the pitching moment coefficient slope per radian

$\{C_{m_q} + C_{m_{\dot\alpha}}\}$ dynamic stability coefficient (assumed constant over an oscillation cycle) $[\partial C_m/\partial(qd/V) + \partial C_m/\partial(\dot\alpha d/V)]$ per radian; also $= \overline{C_{m_q}}$

d reference length equal to model diameter

g acceleration due to gravity

I model moment of inertia about a transverse axis at center of gravity

m mass of model

M Mach number

P pressure

q angular pitching velocity

q_∞ free-stream dynamic pressure

Re_d free-stream Reynolds number based on model diameter

V velocity of model relative to the media, i.e., reference point moving with the flow

X position of model relative to the media, i.e., reference point moving with the flow

α angle of attack

α_0 initial oscillation amplitude

$\bar\alpha_0$ mean oscillation amplitude

β inverse scale height

λ damping parameter

ψ angle of yaw

θ total angle of attack, $\tan^2\theta = \tan^2\alpha + (\tan^2\psi/\cos^2\alpha)$

η total angle-of-attack envelope

ρ gas density

ω oscillation frequency, rad/s

Ω distance oscillation frequency, radian/distance X traveled

$(\cdot)$ derivative with respect to time

$(\cdot\cdot)$ second derivative with respect to time

$(\ )'$ derivative with respect to X

Subscripts

0 conditions at zero distance or zero altitude

eff effective

X conditions at distance equal to X

∞ free-stream conditions

E entry conditions

Configurations

$M_{(\_)}$ cone half-angle of (—) model

$N_{(\_)}$ nose radius of (—)% of model diameter

$E_{(\_)}$ edge radius of (—)% of model diameter

References

1. Marko, W. J., "Dynamic Stability of High Drag Planetary Entry Vehicles at Transonic Speeds," Paper 69-105, presented at the AIAA Seventh Aerospace Sciences Meeting, New York, Jan. 20–22, 1969.

2. Dayman, B., Jr., *Free-Flight Testing in High-Speed Wind Tunnels,* NATO-AGARD, Paris, May 1966, AGARDograph 113. Available through the National Aeronautics and Space Administration, Washington, D.C.

3. Holway, H., Herrera, G., and Dayman, B., Jr., *A Pneumatic Model Launcher for Free-Flight Testing in a Conventional Wind Tunnel,* Technical Memorandum 33-177. Jet Propulsion Laboratory, Pasadena, Calif., July 30, 1964.

4. Prislin, R. H., *Free-Flight and Free-Oscillation Techniques for Wind Tunnel Dynamic Stability Testing,* Technical Report 32-878. Jet Propulsion Laboratory, Pasadena, Calif., Mar. 1, 1966.

5. Prislin, R. H., and Holway, H. P., "A Wind Tunnel Free Flight Testing Technique for Nonplanar Motion of Spinning Models," Paper 66-774, presented at the AIAA Aerodynamic Testing Conference, Los Angeles, Calif., September 1966.

6. Knoell, A. C., *Environmental and Physical Effects on the Response of Balsa Wood as an Energy Dissipator,* Technical Report 32-944. Jet Propulsion Laboratory, Pasadena, Calif., June 15, 1966.

7. *Schlieren Photography,* Kodak Scientific and Technical Data. Eastman Kodak Company, Rochester, N.Y., 1960.

8. Marko, W. J., *Static Aerodynamic Characteristics of Three Blunted Sixty-Degree Half-Angle Cones at Mach Numbers From 0.60 to 0.30,* Technical Report 32-1298. Jet Propulsion Laboratory, Pasadena, Calif., July 1, 1968.

9. Krumins, M. V., "Drag and Stability of Mars Probe/Lander Shapes," *J. Spacecraft Rockets,* Vol. 4, No. 8, August 1967.

10. Bendura, R. J., *Low Subsonic Static and Dynamic Stability Characteristics of Two Blunt 120° Cone Configurations,* NASA TN D-3853. National Aeronautics and Space Administration, Washington, D.C., 1967.

11. Whitlock, C. H., and Bendura, R. J., *Dynamic Stability of a 4.6-Meter-Diameter 120° Conical Spacecraft at Mach Numbers from 0.78 to 0.48 in a Simulated Martian Environment,* NASA TN D-4858. Langley Research Center, Langley Station, Hampton, Va., May 1968. Also, National Aeronautics and Space Administration, Washington, D.C.

12. Whitlock, C. H., Bendura, R. J., and Henning, A. B., "Dynamic Stability Characteristics of Large-Size 120° Blunted Conical Spacecraft in a Simulated Martian Environment," Paper 69-104, presented at the AIAA Seventh Aerospace Sciences Meeting, New York, Jan. 20–22, 1969.

13. Sammonds, R. I., "Correlation of Free-Flight Dynamic-Stability Data Obtained in Several Different Facilities," Paper presented at the Third Technical Workshop on Dynamic Stability Problems, Ames Research Center, Moffett Field, Calif., Nov. 4–7, 1968.

References (contd)

14. Jaffe, P., *A Generalized Approach to Dynamic-Stability Flight Analysis,* Technical Report 32-757. Jet Propulsion Laboratory, Pasadena, Calif., July 1, 1965.

15. Walker, B., and Weaver, R. W., *Static Aerodynamic Characteristics of Blunted Cones in the Mach-Number Range From 2.2 to 9.5,* Technical Report 32-1213. Jet Propulsion Laboratory, Pasadena, Calif., Dec. 1, 1967.

16. Shirley, D. L., and Misselhorn, J. E., "Instability of High-Drag Planetary Entry Vehicles at Subsonic Speeds," *J. Spacecraft Rockets,* Vol. 5, No. 10, October 1968.

NASA — JPL — Coml., L.A., Calif.